Available online at www.sciencedirect.com

ScienceDirect

Geochimica et Cosmochimica Acta 217 (2017) 95–111

Geochimica et Cosmochimica Acta

www.elsevier.com/locate/gca

Thermal equilibration of iron meteorite and pallasite parent bodies recorded at the mineral scale by Fe and Ni isotope systematics

Stepan M. Chernonozhkin [a,b], Mona Weyrauch [c], Steven Goderis [a,b,*], Martin Oeser [c], Seann J. McKibbin [b], Ingo Horn [c], Lutz Hecht [d], Stefan Weyer [c], Philippe Claeys [b], Frank Vanhaecke [a]

[a] *Ghent University, Department of Analytical Chemistry, Campus Sterre, Krijgslaan 281–S12, 9000 Ghent, Belgium*
[b] *Vrije Universiteit Brussel, Analytical, Environmental, and Geo-Chemistry, Pleinlaan 2, 1050 Brussels, Belgium*
[c] *Leibniz Universität Hannover, Institute of Mineralogy, Callinstrasse 3, 30167 Hannover, Germany*
[d] *Museum für Naturkunde, Leibniz Institute for Evolution and Biodiversity Science, Invalidenstrasse 43, 10115 Berlin, Germany*

Received 6 January 2017; accepted in revised form 9 August 2017; available online 19 August 2017

Abstract

In this work, a femtosecond laser ablation (LA) system coupled to a multi-collector inductively coupled plasma-mass spectrometer (*fs*-LA-MC-ICP-MS) was used to obtain laterally resolved (30–80 μm), high-precision combined Ni and Fe stable isotope ratio data for a variety of mineral phases (olivine, kamacite, taenite, schreibersite and troilite) composing main group pallasites (PMG) and iron meteorites. The stable isotopic signatures of Fe and Ni at the mineral scale, in combination with the factors governing the kinetic or equilibrium isotope fractionation processes, are used to interpret the thermal histories of small differentiated asteroidal bodies. As Fe isotopic zoning is only barely resolvable within the internal precision level of the isotope ratio measurements within a single olivine in Esquel PMG, the isotopically lighter olivine core relative to the rim ($\Delta^{56/54}Fe_{rim\text{-}core} = 0.059‰$) suggests that the olivines were largely thermally equilibrated. The observed hint of an isotopic and concentration gradient for Fe of crudely similar width is interpreted here to reflect Fe loss from olivine in the process of partial reduction of the olivine rim. The ranges of the determined Fe and Ni isotopic signatures of troilite ($\delta^{56/54}Fe$ of −0.66 to −0.09‰) and schreibersite ($\delta^{56/54}Fe$ of −0.48 to −0.09‰, and $\delta^{62/60}Ni$ of −0.64 to +0.29‰) may result from thermal equilibration. Schreibersite and troilite likely remained in equilibrium with their enclosing metal to temperatures significantly below their point of crystallization. The Ni isotopic signatures of bulk metal and schreibersite correlate negatively, with isotopically lighter Ni in the metal of PMGs and isotopically heavier Ni in the metal of the iron meteorites analyzed. As such, the light Ni isotopic signatures previously observed in PMG metal relative to chondrites may not result from heterogeneity in the Solar Nebula, but rather reflect fractionation in the metal-schreibersite system. Comparison between the isotope ratio profiles of Fe and Ni determined across kamacite-taenite interfaces ($\Delta^{56/54}Fe_{kam\text{-}tae} = -0.51$ to $-0.69‰$ and $\Delta^{62/60}Ni_{kam\text{-}tae} = +1.59$ to $+2.50‰$) and theoretical taenite sub-solidus diffusive isotopic zoning broadly constrain the cooling rates of Esquel, CMS 04071 PMGs and Udei Station IAB to between ~25 and 500 °C/Myr.
© 2017 Elsevier Ltd. All rights reserved.

Keywords: Pallasites; Iron meteorites; Fe and Ni stable isotope ratios; Core formation; Schreibersite

* Corresponding author at: Vrije Universiteit Brussel, Analytical, Environmental, and Geo-Chemistry, Pleinlaan 2, 1050 Brussels, Belgium.
E-mail address: Steven.Goderis@vub.be (S. Goderis).

http://dx.doi.org/10.1016/j.gca.2017.08.022
0016-7037/© 2017 Elsevier Ltd. All rights reserved.

1. INTRODUCTION

In the course of planetary evolution, mountain-sized planetesimals of primitive composition accreted, grew *via* a series of collisions to form planetary embryos, differentiated and ultimately evolved into terrestrial planets with rocky crusts, mantles and metal cores. The thermal and differentiation histories of these accreting small planetary bodies have direct bearing on the dynamic models of planetary embryo growth and core formation (Rubie et al., 2015), as well as on the final bulk composition of the planet (Drake and Righter, 2002). A deeper understanding of the thermal evolution of these discrete blocks of planets sheds light on the pathways of planetary growth. Iron meteorites and main group pallasites (PMGs) are believed to originate from deep within small highly differentiated bodies, with segregated metal cores and silicate mantles (Greenwood et al., 2006), representing the earliest stages of planetary formation. Most iron meteorites are thought to sample the Fe-Ni cores of catastrophically disrupted differentiated asteroids, as most of these show fractional crystallization trends in their element compositions (Scott, 1972). PMGs consist of nearly equal amounts of Fe-Ni metal and olivine and the trace element contents of PMG metal are consistent with an end-member composition of the fractional crystallization sequence observed for IIIAB iron meteorites (Wasson, 2016). Although the formational history of pallasites remains heavily debated, these meteorites likely represent mixtures of Fe-Ni metal from a core and mantle-derived olivine from the core-mantle boundary of differentiated asteroids (Boesenberg et al., 2012; McKibbin et al., 2013). Trace element systematics and zoning in PMG olivine have been used to constrain the magmatic histories experienced by these olivines before the olivine-metal mixing event (McKibbin et al., 2013). However, as the olivine compositions largely equilibrated after their mixing with molten metal, the late-stage thermal histories of PMGs might have been recorded by the metal-olivine element and isotope partitioning (Reed et al., 1979; Poitrasson et al., 2005; Chernonozhkin et al., 2016), potentially reflected in PMG elemental and isotopic zoning (Miyamoto, 1997; Tomiyama and Huss, 2006; Dauphas, 2007). If the olivines of PMGs equilibrated chemically and isotopically, the elemental and isotopic olivine-metal fractionation factors available in literature may be used to calculate equilibration temperatures, and the elemental and isotopic distributions can be used as geothermometers (Valley, 2001). On the other hand, if full equilibrium between the adjacent minerals was not achieved, the diffusive profiles of elemental concentrations and isotope ratios from the olivine cores to the rims can be used to constrain the cooling rates of the parent body and to refine our understanding of the nature of the processes taking place during the thermal evolution of the olivine through modeling (Miyamoto, 1997; Sio et al., 2013; Oeser et al., 2015; Sio and Dauphas, 2017).

Schreibersite ($(Fe,Ni)_3P$) and troilite (FeS) are minor minerals contained in iron meteorites and PMGs, which contain the main fractions of the P and S present in asteroidal metal cores. Troilite, similar to schreibersite, is thought to have a magmatic origin, as it is assumed to have been exsolved from metal melts at eutectic temperatures due to the incompatible nature of S and P as fractional crystallization of the metal core proceeded. Troilite-metal Fe isotope fractionation factors ($\Delta^{56/54}Fe_{metal\text{-}troilite} = \delta^{56/54}Fe_{metal} - \delta^{56/54}Fe_{troilite}$) have previously been shown to correlate with metallographic cooling rates (Williams et al., 2006). This relation indirectly indicates a thermodynamic control of Fe isotope fractionation in troilite, because closure temperatures (T_c), a principal parameter controlling the magnitude of the equilibrium isotope fractionation between phases, depend on the cooling rates (dT/dt) *via* the Dodson equation (*cf.* Fig. 7 and the corresponding discussion in Valley, 2001; Dodson, 1973):

$$T_c = \frac{R}{E ln(A\tau D_0/a^2)}; \quad \tau = -\frac{RT^2}{EdT/dt} \tag{1}$$

The closure temperature determines the effective temperature below which exchange effectively ceases. In Eq. (1), R denotes the gas constant, E and D_0 are the activation energy and pre-exponent of the diffusion, a is a characteristic diffusion size and A is a numerical constant. The observation that the troilite-metal fractionation ($\Delta^{56/54}Fe_{troilite\text{-}metal}$) depends on the cooling rate (Williams et al., 2006) enables the Fe-FeS system to be used as an isotope geothermometer, relying on the thermodynamic parameters, recently determined for Fe in troilites by nuclear resonance inelastic X-ray scattering (NRIXS, Dauphas et al., 2012).

After the molten Fe-Ni metal in the core is fully crystallized, the cooling of the parent body proceeds and the *fcc* crystal structure, thermodynamically stable at temperatures above ~800 °C, starts to nucleate to form *bcc* Ni-poor α-iron (kamacite) and *fcc* Ni-rich γ-iron (taenite) (Goldstein and Ogilvie, 1965). Nickel concentration profiles across taenite lamellae of meteorites, formed *via* sub-solidus diffusion, can thus be used to determine meteorite cooling rates. Previous studies showed that Fe and Ni isotopic signatures of Fe-Ni metal in iron meteorites and pallasites exhibit a surprisingly large range to have formed following an equilibrium process, and this probably suggests a process of kinetic nature for kamacite-taenite formation *via* subsolidus diffusion ($\Delta^{56/54}Fe_{kam\text{-}tae}$ values of up to – 0.3‰, see Poitrasson et al., 2005; Weyer et al., 2005; Horn et al., 2006; Williams et al., 2006; Cook et al., 2007). Diffusion drives Fe and Ni isotope fractionation in iron meteorites, and isotope ratio profiles may potentially be used to constrain the cooling process of the parent body by modeling the observed degree of diffusion in the metal (Dauphas, 2007).

The main goal of this work is to provide high-precision *in situ* stable Fe and Ni isotope ratio data for relevant accessory mineral phases in PMGs and iron meteorites, including laterally resolved isotope ratio profiles to shed light on the cooling and crystallization histories of metal-rich meteorite parent bodies at the mineral scale and to further constrain the formation and thermal evolution of these small differentiated asteroidal bodies. The ability of femtosecond laser ablation to accomplish largely matrix-independent sampling without laser-related isotope fractionation removes the necessity of matrix correction, which

is often complex in the case of nanosecond LA systems (Sio et al., 2013). Due to its longer duration, the interaction of a nanosecond laser pulse with a sample is affected by the nature of the material, leading to changes in the formation mechanism of the sample aerosol (Povarnitsyn et al., 2007). As a result, nanosecond pulses result in increased evaporation, melting, aerosol losses and laser-induced isotopic fractionation (Jackson and Günther, 2003). This is not the case for femtosecond LA-systems, which practically do not induce laser-induced isotope fractionation (Horn and von Blanckenburg, 2007). The ability to use an admixed internal standard, nebulized from a solution, for internal correction for instrumental mass discrimination permits high-precision *in situ* (*i.e.,* directly accessing the solid material) measurements of isotope ratios, highly in demand in geo- and cosmochemistry. In comparison to pneumatic nebulization MC-ICP-MS, application of *fs*-LA sampling enables the analysis of pure sub-mm accessory minerals without potential mixing with other phases. The *in situ* sampling strategy is used in this work to unravel the equilibration histories of the mineral phases.

2. MATERIALS AND METHODS

2.1. Samples

Two iron meteorites (Chinga IVB ungrouped and Sikhote-Alin IIB) were obtained from the Central Siberian Geological Museum, V. S. Sobolev Institute of Geology and Mineralogy, Russia. These iron meteorites have previously been characterized for their major and trace element concentrations, while bulk and microdrilled fractions of these meteorites have also been analyzed for their Fe and Ni isotope ratios in previous work (Chernonozhkin et al., 2014, 2015, 2016). A section of the PMG CMS 04071 was obtained from the Antarctic meteorite collection of the US National Aeronautics and Space Administration (NASA), while the Esquel, Brahin, Fukang, Seymchan and Springwater PMGs, as well as Udei Station IAB, were purchased from meteorite vendors. Brenham PMG was provided by the Research School of Earth Sciences, Australian National University. The samples were characterized for their Fe and Ni element distributions using micro X-ray fluorescence spectrometry (μXRF). The acquired 2 D μXRF element distribution maps distinguish mineral phases in the targeted meteorites and enable ideal locations for high-precision isotopic analysis using fs-LA-MC-ICP-MS to be selected.

2.2. Reference materials

The certified isotopic reference material IRMM-014 Fe was used as an external standard in a sample-standard bracketing sequence to correct for instrumental mass discrimination when measuring Fe isotope ratios in metal, troilite and schreibersite. When measuring Fe isotope ratios in olivines of PMGs, USGS BCR-2G was used as an external isotopic standard. First, reference values for the latter were adapted from Oeser et al. (2014), and subsequently the measured values for the sample were re-calculated with respect to IRMM-014. Although no matrix effects have been observed during femtosecond laser ablation sampling, BCR-2G was preferred over IRMM-014 because the Fe concentrations of the former fit closer to those of the measured olivines. When Fe isotope ratios were measured, the Ni certified isotopic reference material NIST SRM 986 was used as an internal standard, added to the laser-generated aerosol *via* pneumatic nebulization. Throughout this study, low alloy steel NIST SRM 1226 with 5.42 wt% Ni was used as an in-house external Ni isotopic standard in a sample-standard bracketing sequence to correct Ni isotope ratio data for instrumental mass discrimination, following an analytical protocol of Weyrauch et al., 2017. The δ-notations of Ni were then recalculated with respect to NIST SRM 986. The Ni isotopic composition of NIST SRM 1226 was determined relative to NIST SRM 986 *via* solution nebulization MC-ICP-MS at the Leibniz Universität Hannover (offset of $\delta^{62/60}$Ni from NIST SRM 986 is −0.28‰, Weyrauch et al., 2017). When Ni isotope ratios were measured, the Cu reference material NIST C125-1 was used as an internal standard, added to the laser-generated aerosol *via* pneumatic nebulization. Quality control materials for Fe include ML3B-G (flux-free basalt glass MPI-DING SRM) and high-purity Fe metal (99.995% Fe, Puratronic, Johnson Matthey, lot No. FE495007IF2), which have previously been characterized for their Fe isotopic compositions (Horn et al., 2006; Oeser et al., 2014).

2.3. Micro X-ray fluorescence spectrometry (μXRF) and electron microprobe analysis (EMPA)

Two-dimensional element distribution maps of the entire thick sections of the iron meteorites and PMGs were obtained using a Bruker M4 Tornado XRF instrument at the Vrije Universiteit Brussel, equipped with a 30 W Rh-anode X-ray source (50 kV operating voltage, 150 μA operating current) and a Be side-window. In this instrument, the X-rays are focused to a 25 μm spot (measured for Mo K_α) using a polycapillary lens. The instrument is equipped with two silicon drift detector (SDD) spectrometers (30 mm^2, 145 eV energy resolution for Mn Ka), placed symmetrically relative to the sample. Measurements were performed under a vacuum of 20 mbar. To acquire 2D elemental distribution maps, a motorized sample stage moves at a speed of 25 mm s^{-1} (1 ms per pixel), scanning the surface during 8 consecutive cycles (total acquisition time of approximately 3–5 h). Quantitative EMPA of the olivines of PMGs was performed using a JEOL JXA-8500F electron microprobe at the Museum für Naturkunde in Berlin. This microprobe is equipped with a field emission cathode, five wavelength-dispersive spectrometers and an energy-dispersive spectrometer (the latter is only used for preliminary imaging). A focused beam with a current of 50 nA at 15 kV accelerating voltage was utilized. K_α peak measurements were made for Si, Al, Mg, P (TAP), Ti, Mn (PETJ), Ni, Ca (PETH), Cr and Fe (LIFH) with peak/background times of 20/10, 40/20, 20/10, 40/20, 40/20, 20/10, 30/15, 30/15, 40/20 and 20/10 s, respectively, and backgrounds measured on both sides of the peaks. Standardization was performed using internationally certified natural mineral standards from

the Smithsonian and Astimex. Matrix effects were corrected for using the built-in JEOL ZAF routine. For more details on the μXRF and EMPA setup and the corresponding procedures, the reader is referred to Chernonozhkin et al. (2016) and Van Roosbroek et al. (2015), respectively.

2.4. In situ isotopic analysis

Fe and Ni isotope ratios were measured using a combination of a femtosecond laser ablation system and a Thermo Scientific (Bremen, Germany) Neptune Plus MC-ICP-MS unit at the Institute of Mineralogy of the Leibniz Universität Hannover (Germany). The in-house built LA-system is based on a 100 femtosecond Ti-sapphire regenerative amplifier (Solstice, Spectra-Physics, Santa Clara, CA, USA) with a fundamental IR wavelength of 775 nm, which was consecutively frequency-quadrupled, thus resulting in an output laser beam with a UV wavelength of 194 nm. The final output energy is ~3.2 mJ pulse^{-1} at a fundamental wavelength of 775 nm, resulting in a pulse energy of 70 μJ at a wavelength of 194 nm. The duration of the laser pulse was determined to be 100–200 fs. The frequency of the laser pulses can be varied between 2 and 500 Hz, and was selected to be in the range of 10–40 Hz during the analyses. The laser spot size and the frequency of the laser pulses were adjusted before each analysis to achieve intensities for the samples and bracketing standards within a ±5% range. For details on the design of the LA-unit, we refer to Horn et al. (2006) and Oeser et al. (2014). Laser sampling was performed by ablating ~400 μm long lines, typically placed parallel to straight margins of the target minerals, while recording the transient MC-ICP-MS signals (see Figs. 1 and 2 and supplementary material for the locations and spacing of the analyses). Line scans were preferred over spot analyses because they allow for longer acquisition times at constant intensity, necessary for high-precision isotope ratio measurements, while preserving the lateral resolution in one dimension. The absence of significant laser-related isotope fractionation was confirmed in previous studies for olivine and metal matrixes (Horn et al., 2006; Steinhoefel et al., 2009; Oeser et al., 2014; Weyrauch

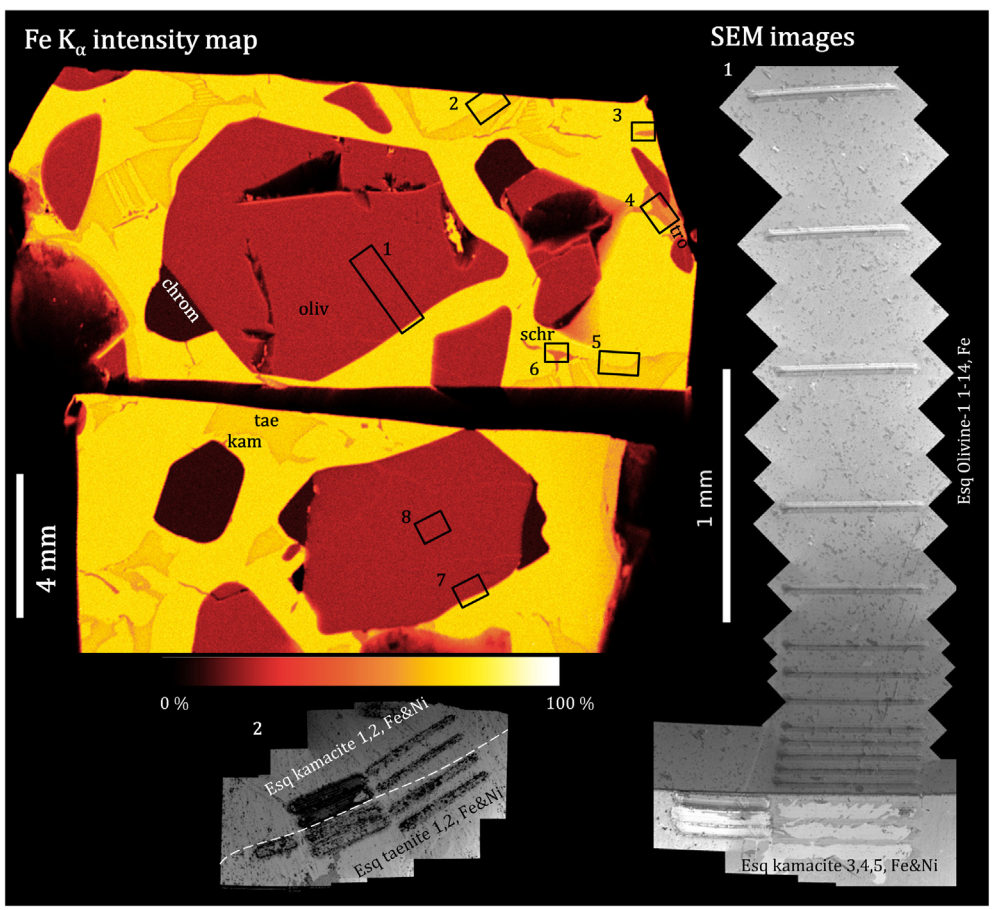

Fig. 1. Top left – Fe K_α intensity distribution map of a thick section of Esquel PMG as determined *via* μXRF. The mineral phases are denoted as follows: oliv – olivine, kam – kamacite, tae – taenite, chrom – chromite, schr – schreibersite and tro – troilite. The numbered black rectangles denote the locations where the Fe and Ni isotope ratios were measured *in situ via fs*-LA-MC-ICP-MS. Right and bottom – examples of laser ablation tracks in kamacite, taenite and olivine imaged using scanning electron microscopy (SEM). The numerical data for these labeled laser pits resulting from *fs*-LA-MC-ICP-MS analysis can be found in Supplementary Table S1. The same μXRF image with more details of the laser ablation tracks can be found as Supplementary Fig. S1.

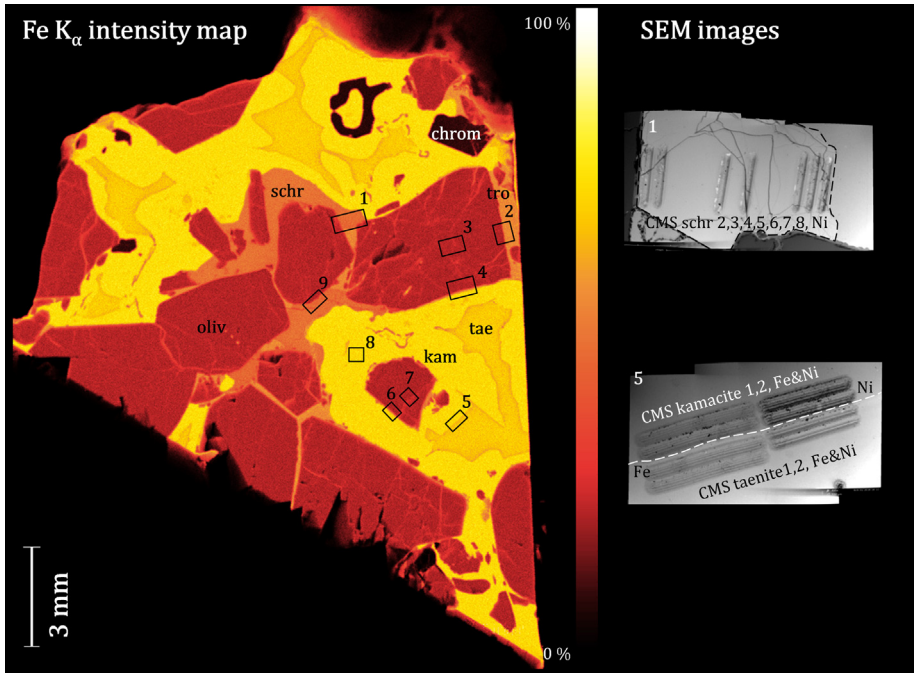

Fig. 2. CMS 04071 PMG, *cf.* Fig. 1. The same μXRF image with more details of laser ablation tracks can be found as Supplementary Fig. S2.

et al., 2017). The laser-generated aerosol is carried away out of the ablation cell using He, and Ar is admixed downstream of the LA-unit. The internal standard solution (5 mg L^{-1} Ni in the case of Fe isotopic analysis and 0.5 mg L^{-1} Cu in the case of Ni isotopic analysis) was added to the sample aerosol *via* pneumatic nebulization accomplished with an ESI PFA-ST nebulizer and a quartz glass spray chamber (double-pass Scott-design). The Thermo Scientific Neptune Plus MC-ICP-MS unit was operated in high mass resolution mode (resolving power = 9000) and equipped with a high-efficiency 'jet' interface. The transient signal was acquired for 180 cycles, with an integration time of 1.049 s, while the gas blank was taken before the actual sample ablation during 30 cycles. The instrumental mass discrimination was corrected for using a combination of internal correction, relying on Russell's law, and external correction in a sample-standard bracketing approach. For Fe isotopic analysis of phases containing Ni, an interpolation of Ni isotope ratios of the internal standard was done between the 30 cycles of gas blank preceding the sample and the first 30 cycles of the following run. The interpolated Ni isotope ratios were then used to correct for instrumental mass discrimination of the Fe isotope ratio data. Following internal mass bias correction, the isotope ratios are reported as delta (δ) values, relative to the bracketing reference material to correct for minor drift in the instrumental parameters:

$$\delta^{x/60}Ni = \left[\frac{(^{x}Ni/^{60}Ni)_{Cucorr,smp}}{(^{x}Ni/^{60}Ni)_{Cucorr,NISTSRM986}} - 1\right] \cdot 1000 \quad (2)$$

$$\delta^{x/54}Fe = \left[\frac{(^{x}Fe/^{54}Fe)_{Nicorr,smp}}{(^{x}Fe/^{54}Fe)_{Nicorr,IRMM014}} - 1\right] \cdot 1000 \quad (3)$$

where x is 61 or 62 for Ni and 56 or 57 for Fe, and the subscripts denote that the ratios were first corrected internally according to Russell's law (Russell et al., 1978). For more details on the measurement protocol, the instrument settings and the correction for instrumental mass discrimination, the reader is referred to Oeser et al. (2014, 2015) and Weyrauch et al. (2017).

3. RESULTS

3.1. Mineral and element characterization

Entire thick sections of all meteorite samples were first characterized using 2D element mapping *via* μXRF to find optimal locations for Fe and Ni *in situ* isotopic analysis. The K_α intensities of Fe, Ni, P, S, Cr and Ca were used to identify kamacite, taenite, olivine, schreibersite, chromite and troilite mineral phases. Two-dimensional intensity maps of the Fe K_α signal for Esquel and CMS 04071 PMGs together with the selected locations for *in situ* Fe and Ni isotopic analyses *via fs*-LA-MC-ICP-MS are presented in Figs. 1 and 2, respectively.

The average Fa# (Fa# = FeO/[FeO + MgO]·100 at.%) determined *via* EMPA for the olivines of the PMGs is 11.45 at.% for CMS 04071, 10.98 at.% for Brahin, 13.29 at.% for Fukang, 11.47 at.% for Brenham, 11.78 at.% for Imilac, 11.17 at.% for Esquel and 10.58 at.% for Seymchan, in full agreement with the previously published values for these meteorites (Supplementary Table S2). No resolvable concentration gradients within 1–2 mm from the olivine rim were found for any of the major elements in 6 PMGs. The olivine of Esquel PMG is the only mineral phase to show Fa# zoning (Fig. 3C). This olivine, referred to as

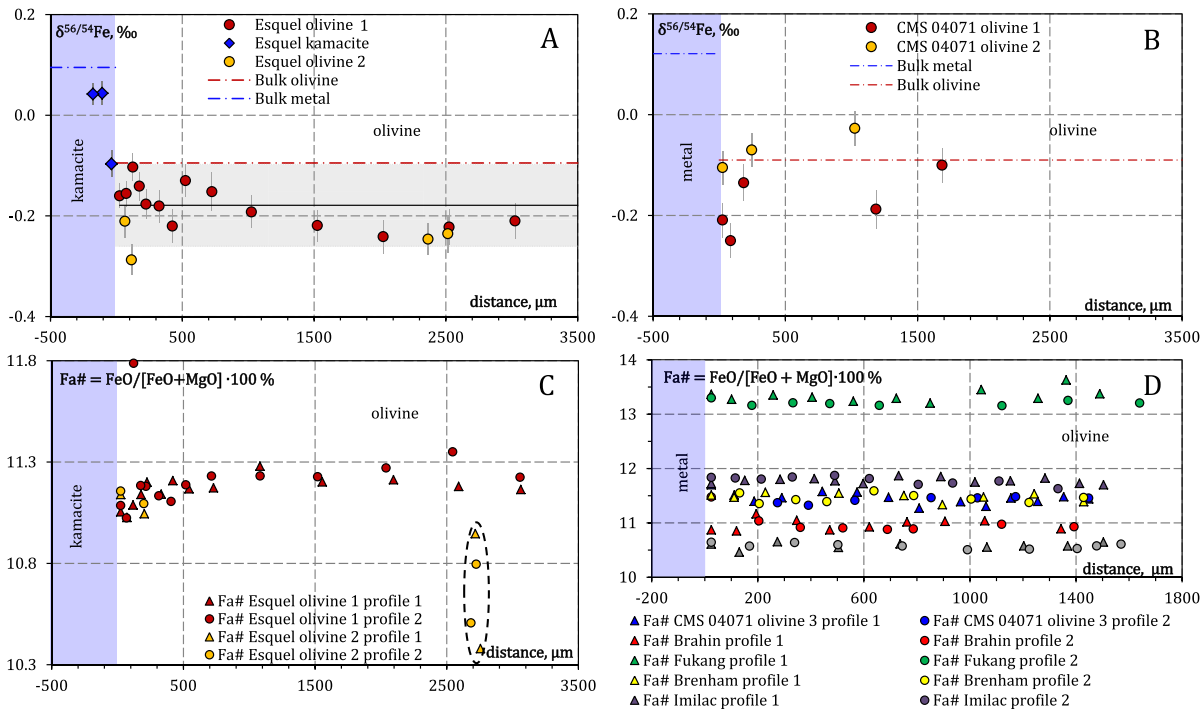

Fig. 3. A, B – Fe stable isotope ratio profiles for olivines of Esquel and CMS 04071, respectively, measured next to the olivine-metal contact, with distance x = 0 corresponding to the olivine margin. The laser spot diameter applied is 40 µm for olivines and 70 µm for the metal phase, with laser lines ablated closely to each other (40 µm and 70 µm displacement for olivines and the metal phase, respectively). The measurements of Esquel kamacite (indicated by blue diamonds) are located adjacent to the profile of Esquel olivine 1, represented by red circles (see appendix). Error bars represent ±1 SD of a single measurement. The Fe isotope ratios for bulk olivine and metal were measured *via* pneumatic nebulization MC-ICP-MS after acid digestion of the meteorite samples and chromatographic Fe isolation at Ghent University, Belgium (Chernonozhkin et al., 2016). The black line and grey bar represent the mean $\delta^{56/54}$Fe with ±2 standard deviations of Esquel olivine 1. Note that this is different from Fig. 5, where the mean $\delta^{56/54}$Fe of all olivine measurements is shown. C – EMPA Fa# profiles of Esquel olivine 1 and olivine 2, measured at both sides of the laser traces of the Fe isotopic profile. D – EMPA Fa# profiles of olivines of six other PMG, measured next to the olivine-metal rim, with no significant zoning. (For interpretation of the references to colour in this figure legend, the reader is referred to the web version of this article.)

Esquel olivine 1, has a Fa# of 11.11 ± 0.14 at.% (2SD) in the rim and 11.23 ± 0.10 at.% (2SD) in its core.

3.2. Fe isotopic analysis

The results of the Fe and Ni *in situ* fs-LA-MC-ICP-MS isotope ratio determinations are summarized in Fig. 5. The initial isotopic composition of undifferentiated material in the early Solar System is represented by chondritic meteorites (*cf.* compilations by Beard and Johnson, 2004; Barrat et al., 2015). A frequency distribution of 77 chondrite $\delta^{56/54}$Fe values from literature is presented in Fig. 4, showing an average value of 0.00 ± 0.10‰ (2SD).

3..2.1. Fe in olivine

The average of $\delta^{56/54}$Fe values measured *in situ* for olivines of PMGs are in agreement with the results for the same meteorites *via* pneumatic nebulization MC-ICP-MS (Chernonozhkin et al., 2016). Olivines of PMGs measured *in-situ* in this work show light $\delta^{56/54}$Fe isotopic signatures ($\delta^{56/54}$Fe of −0.29 to −0.03‰), at the lower end of the chondritic range and slightly lighter than previously reported by Weyer et al. (2005), who observed chondritic $\delta^{56/54}$Fe for other PMG samples. Small deviations between the bulk and *in situ* isotopic signatures to slightly heavier bulk values may relate to the inter-laboratory nature of these datasets, *e.g.*, linked to the use of an USGS silicate reference glass (BCR-2G) as an auxiliary in-house Fe isotopic standard for the analysis of olivine with LA-MC-ICP-MS data.

3.2.2. Fe in kamacite and taenite

The average $\delta^{56/54}$Fe values for kamacite of iron meteorites and PMG agree with the range reported in literature for ordinary chondrites, and are in good agreement with the results for bulk metal measured previously (Chernonozhkin et al., 2016) for the same meteorites *via* pneumatic nebulization MC-ICP-MS (see Fig. 4). Although the average $\delta^{56/54}$Fe measured *via fs*-LA-MC-ICP-MS for kamacite of PMG are within the range of the previously reported Fe isotopic compositions of PMGs (see Fig. 4 for a compilation of the literature data), the $\delta^{56/54}$Fe variation within kamacite grains of a single meteorite is larger, up to 0.37‰ (*i.e.*, $\delta^{56/54}$Fe of −0.28 to +0.09‰ in Esquel kamacite). Fe is isotopically heavier in taenite than in kamacite (the largest $\Delta^{56/54}Fe_{kam\text{-}tae}$ observed here is −0.82‰, see

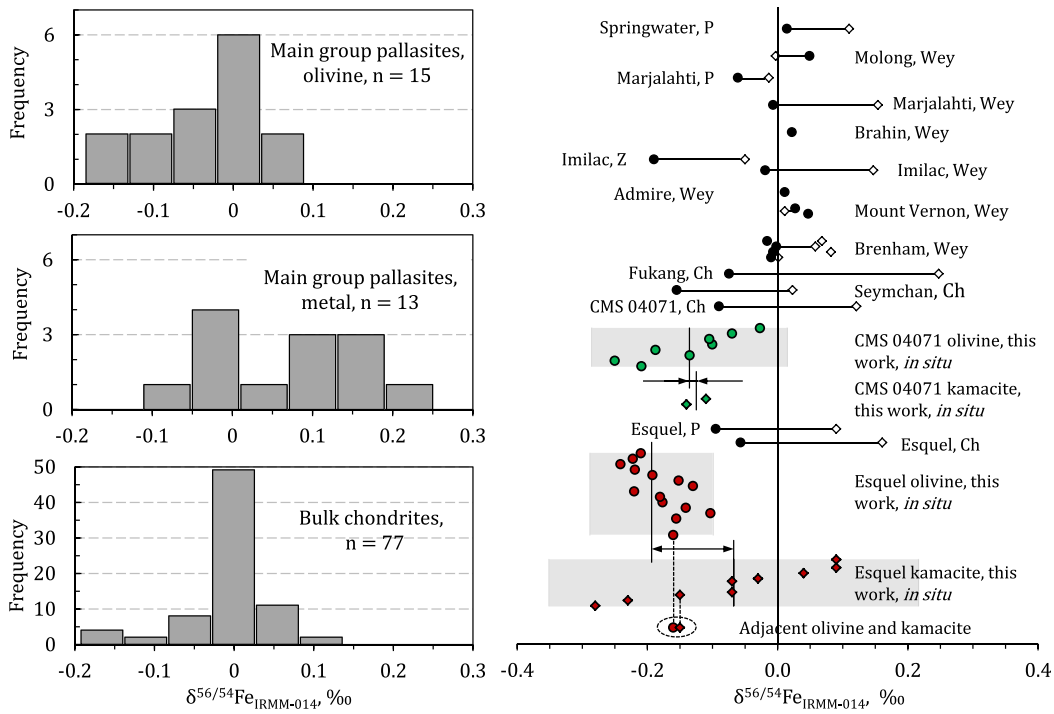

Fig. 4. Compilation of literature $\delta^{56/54}$Fe data (relative to IRMM-014) in the olivines (circles) and metal portions (diamonds) of PMGs. Colored markers represent *in situ* data from this work, with the central lines representing averages and grey bars showing ±2SD. The dimension arrows represent the Fe isotope fractionations between olivine and kamacite: $\Delta^{56/54}Fe_{oliv\text{-}kam}$ for PMG CMS 04071 (0.011‰) and PMG Esquel (0.124‰). The dashed lines show the *in situ* measurements of adjacent olivine and kamacite of PMG Esquel at their margin ($\Delta^{56/54}Fe_{oliv\text{-}kam}$ = 0.010‰). Note that the latter correlate well with previous measurements of the Mount Vernon PMG (Weyer et al., 2005), the Marjalahti PMG (Poitrasson et al., 2005) and experiments on metal-silicate equilibration (Roskosz et al., 2006; Hin et al., 2012). When parallel measurements are reported from the same literature source, only their average is added to the frequency distributions. However, the frequency distributions shown here include measurements of the same meteorite carried out in different labs and therefore, these values likely represent different sections of the meteorite. The data on PMGs are taken from (Ch – Chernonozhkin et al., 2016; P – Poitrasson et al., 2005; Wey – Weyer et al., 2005; Z – Zhu et al., 2001). The data on chondrites is from (Zhu et al., 2001; Poitrasson et al., 2005; Schoenberg and von Blanckenburg, 2006; Needham et al., 2009; Dauphas et al., 2009; Hezel et al., 2010, 2015; Craddock and Dauphas, 2011; Chernonozhkin et al., 2016).

Fig. 6). Previously, Košler et al. (2005) reported kamacite-taenite $\Delta^{56/54}Fe_{kam\text{-}tae}$ fractionation factors of −2.92‰ using nanosecond LA-MC-ICP-MS for iron meteorites. In contrast, Horn et al. (2006) and Weyrauch et al., 2017 found considerably smaller $\Delta^{56/54}Fe_{kam\text{-}tae}$ values of −0.3‰ and −0.45‰ for the IAB Toluca and IAB Canyon Diablo iron meteorites respectively using *fs*-LA-MC-ICP-MS. Similarly, Chernonozhkin et al. (2016) presented $\Delta^{56/54}Fe_{kam\text{-}tae}$ values of up to −0.088‰ for the silicate-bearing iron meteorites and $\Delta^{56/54}Fe_{kam\text{-}tae}$ values of up to −0.19‰ for the IIIAB and IVA iron meteorites. These data were obtained using a protocol that combined sampling using a micro-drill with pneumatic nebulization MC-ICP-MS isotopic analysis.

3.2.3. Fe in troilite and schreibersite

Troilite is characterized by light $\delta^{56/54}$Fe isotopic signatures ($\delta^{56/54}$Fe of −0.66 to −0.09‰) relative to kamacite and taenite of the host meteorite, and schreibersite generally exhibits light $\delta^{56/54}$Fe isotopic signatures relative to chondrites ($\delta^{56/54}$Fe is −0.48 to −0.09‰; Fig. 5). Previously, Poitrasson et al. (2005) and Weyer et al. (2005) observed light Fe isotopic signatures for troilites of PMGs ($\delta^{56/54}$Fe of −0.298 to −0.158‰), but heavy Fe isotopic signatures for schreibersites ($\delta^{56/54}$Fe of +0.156 to +0.244‰).

3.3. Ni isotopic analysis

Relative to Fe, the Ni isotopic composition of chondrites is much less constrained. The chondritic value for $\delta^{60/58}$Ni is currently best defined for ordinary chondrites and is ranging between +0.149 and +0.242‰ relative to NIST SRM 986 (Chernonozhkin et al., 2016). Cook et al. (2007) found the $\delta^{61/58}$Ni of the bulk metal in carbonaceous and ordinary chondrites to range between +0.18 and +0.60‰ relative to NIST SRM 986. Here, one should keep in mind that NIST SRM 986, used as reference for Ni isotope ratio measurements, has shifted from a chondritic isotopic composition during manufacturing by the Mond process (Tanimizu and Hirata, 2006).

The average $\delta^{62/60}$Ni results for kamacite in Sikhote-Alin IIA and Chinga iron meteorites fall within the range

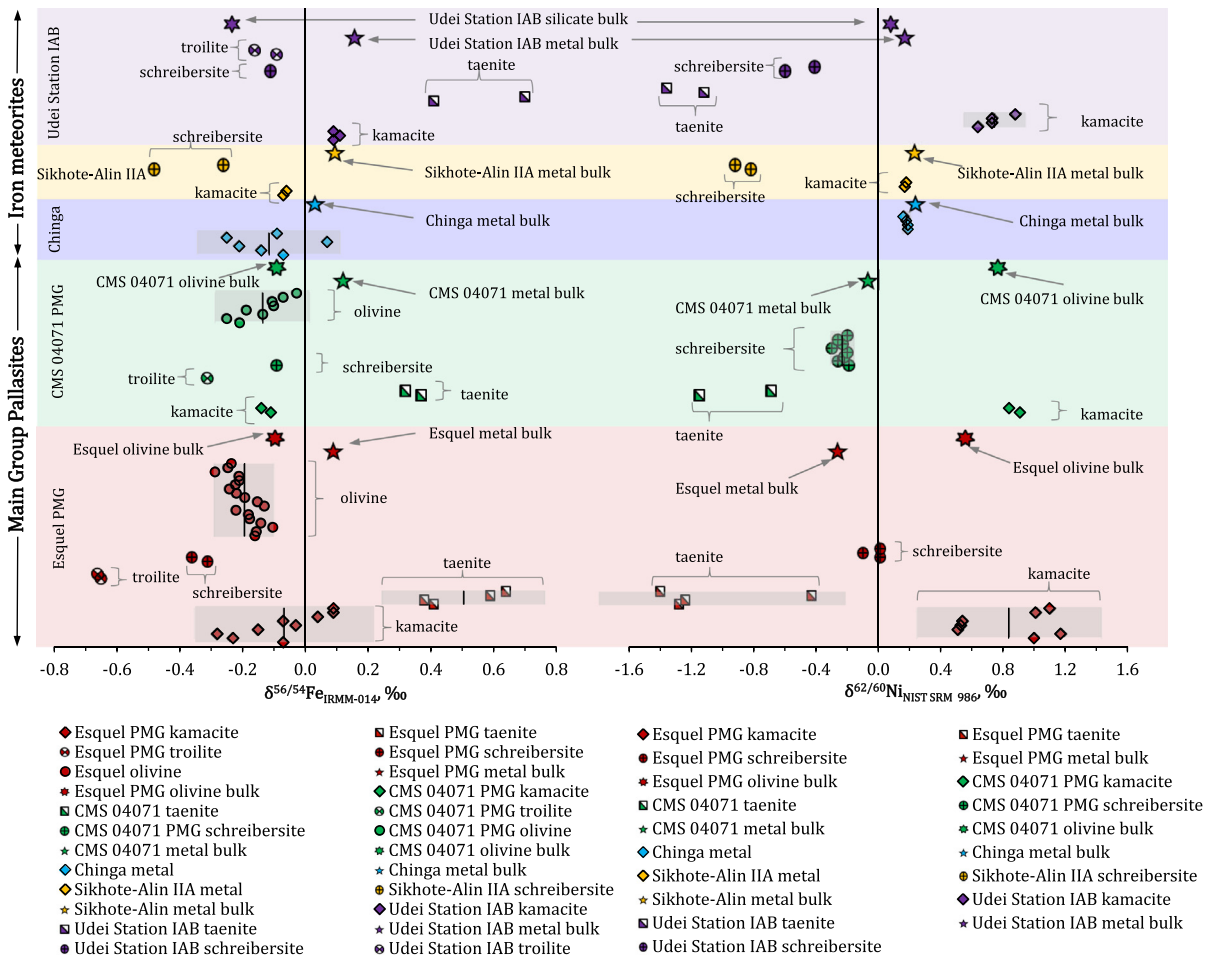

Fig. 5. Stable isotope ratio plots for $\delta^{56/54}$Fe and $\delta^{62/60}$Ni in different mineral phases of 2 PMGs and 3 iron meteorites. Bulk meteorite Ni isotope ratio data, marked by stars, are reported as $\delta^{60/58}$Ni (Chernonozhkin et al., 2016). All the other data represent *in situ* measurements from this work. Given the similar mass difference between the isotopes in the ^{60}Ni-^{58}Ni and ^{62}Ni-^{60}Ni couples, these values are similar. See appendix 2 for numerical data and Figs. 1 and 2 for information on the locations of the laser pits.

of ordinary chondrites. In contrast, the average $\delta^{62/60}$Ni results for kamacite in the Udei Station IAB iron meteorite and PMGs are significantly heavier than the range reported for ordinary chondrites. The average Ni isotopic signatures of the kamacite of Sikhote-Alin IIA and Chinga ungrouped iron meteorites measured *in situ* are in good agreement with the bulk signatures obtained previously using pneumatic nebulization MC-ICP-MS (Chernonozhkin et al., 2016). However, the average Ni isotopic signatures of the metal phases of Udei Station IAB, CMS 04071 PMG and Esquel PMG do not correspond to the previously measured bulk signatures due to large fractionation within kamacite-taenite metal. Nickel in taenite is isotopically lighter than in kamacite; the largest measured kamacite-taenite $\Delta^{62/60}Ni_{kam\text{-}tae}$ fractionation factor for Ni is 2.57‰. Previously, Weyrauch et al., 2017 observed $\Delta^{62/60}Ni_{kam\text{-}tae}$ of 1.08‰ for Canyon Diablo IAB iron meteorite. Nickel isotope ratios were not measured in troilite, because of its low Ni abundances. Schreibersite generally exhibits light $\delta^{62/60}$Ni isotopic signatures relative to chondrites ($\delta^{62/60}$Ni values of −0.64 to +0.29‰, see Fig. 5).

4. DISCUSSION

4.1. Kamacite-taenite isotope ratio profiles

Previous work has demonstrated that the differences in the Fe and Ni isotopic compositions of kamacite (*bcc* α-iron, Ni-poor) and taenite (*fcc*, γ-iron, Ni-rich) are a result of kinetically driven isotope fractionation accompanying the sub-solidus diffusion during formation of the Widmanstätten pattern, when kamacite and taenite form during cooling of the parent body below ~800 °C (Dauphas, 2007; Watson et al., 2016; Weyrauch et al., 2017). Here, profiles of $\delta^{56/54}$Fe and $\delta^{62/60}$Ni across kamacite-taenite interfaces were revealed with a laser beam diameter of 45 to 70 μm in the Udei Station IAB iron meteorite and the PMGs Esquel and CMS 04071 (Fig. 6). Although the formation of Widmanstätten pattern occurs at temperatures below ~800 °C, when the diffusion in silicates no longer takes place in measurable terms, silicate-bearing irons and pallasites may not represent the best samples to study kamacite-taenite formation, since interactions between the metal and

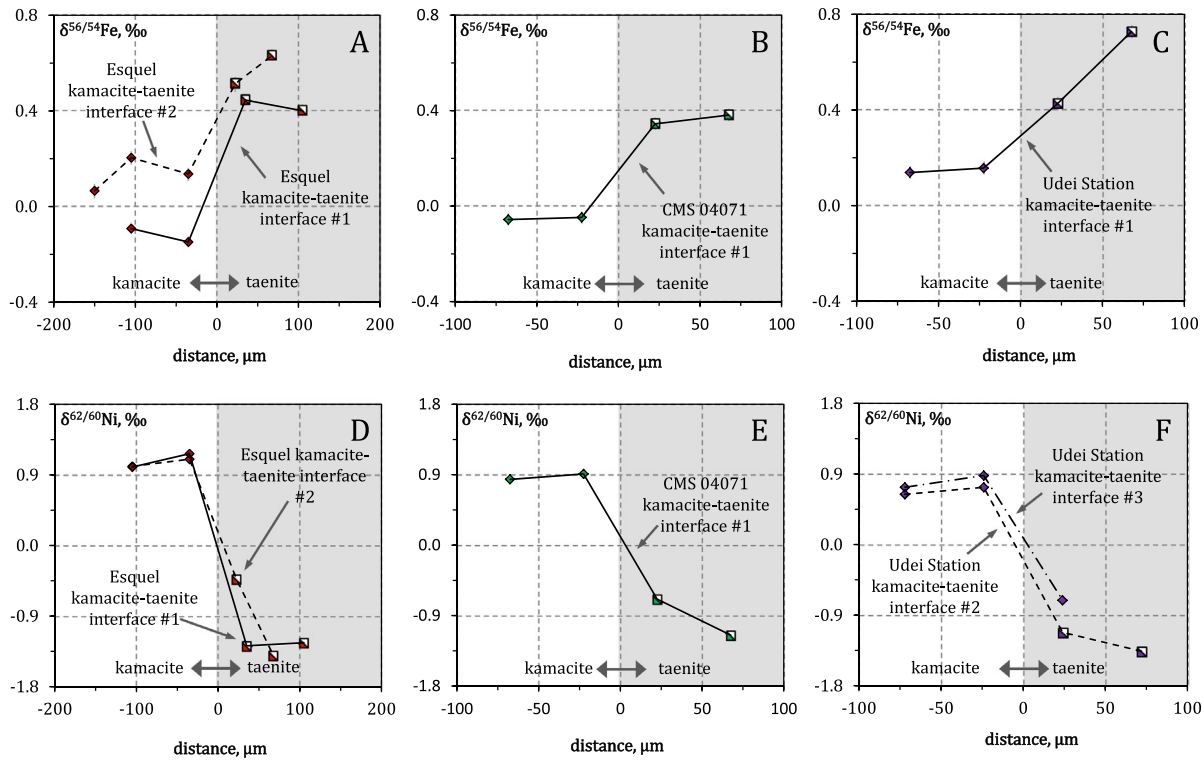

Fig. 6. $\delta^{57/54}$Fe (A–C) and $\delta^{62/60}$Ni (D–F) profiles of kamacite and taenite, measured at the kamacite-taenite interfaces of the Esquel PMG (A, D), CMS 04071 PMG (B, E) and Udei Station IAB iron (C, F). The Fe and Ni isotopic signatures were measured at nearly the same position with respect to the rim (Figs. 1 and 2), *via fs*-LA-MC-ICP-MS. Laser line scans were positioned parallel to the mineral interfaces without gaps between neighboring lines. The lines scanned to characterize the Ni isotope ratio profiles were positioned as closely as possible to those corresponding to the Fe isotope ratio profile in the case of Esquel and CMS 04071. For Udei Station, the $\delta^{57/54}$Fe and $\delta^{62/60}$Ni were measured at different kamacite-taenite interfaces, because of spatial limitations.

silicates may potentially have triggered some local modification of the isotopic budget. Iron meteorites from the formerly designated "magmatic" groups should be preferred for more detailed isotopic studies. The largest measured Fe isotope fractionation between kamacite and taenite for each of the samples studied is $\Delta^{56/54}Fe_{kam\text{-}tae} = -0.78‰$, $-0.56‰$ and $-0.82‰$ for PMG Esquel, PMG CMS 04071 and IAB Udei Station, respectively, while the largest measured kamacite-taenite fractionation for Ni is $\Delta^{62/60}Ni_{kam\text{-}tae} = 2.57‰$, $2.06‰$ and $2.24‰$, respectively. The $\delta^{56/54}$Fe and $\delta^{62/60}$Ni values are negatively correlated in Fe-Ni metal (Fig. 7). This negative correlation and the overall larger fractionation factors for Ni compared to Fe, with similar differences between the isotope masses involved (56/54 and 62/60), agree with a diffusive control on the isotope fractionation. The negative correlation between the Fe and Ni isotopic signatures results from the fact that the directions of Fe and Ni sub-solidus diffusion relative to the kamacite-taenite interface are opposite (Ni moves towards taenite, while Fe moves towards kamacite) (Dauphas, 2007). Except for the Esquel PMG profile (#1; Fig. 6A and D), the highest magnitudes in Fe and Ni isotopic shifts occur with an increasing distance from the kamacite-taenite interface (close to the core of the lamellae), with isotopic shifts of smaller magnitude adjacent to the kamacite-taenite interface. Compared to the modeled diffusive isotope ratio profiles (*cf.* Figs. 8 and 9 of Dauphas, 2007), such measured $\delta^{56/54}$Fe and $\delta^{62/60}$Ni profiles are more similar to the predicted patterns at 650 °C. The isotope ratio profiles predicted by Dauphas (2007) at 450 °C, the temperature at which the Fe-Ni diffusion is virtually frozen in the metal, are different from the patterns measured *in situ* here as the model predicts the largest isotopic shifts in areas adjacent to the kamacite-taenite edge, keeping in mind that with the method used, integrated averages over the area of the laser spot size are reported. Given the extent of isotope fractionation ($\Delta^{56/54}Fe_{kam\text{-}tae} = -0.51$ to $-0.69‰$ and $\Delta^{62/60}Ni_{kam\text{-}tae} = +1.59$ to $+2.50‰$), slow cooling rates (*i.e.* $\leq$25 °C/Myr) are less likely, based on a comparison of the observed profiles with modeled profiles (Dauphas, 2007; Watson et al., 2016). Such slow cooling rates are modeled to result in $\Delta^{62/60}Ni_{kam\text{-}tae}$ values well below 1.5‰. At the same time, based on the lateral patterns of the measured profiles and the magnitude of the measured isotope fractionation, fast cooling rates (*i.e.*, $\geq$500 °C/Myr) are also rather unlikely, as such fast cooling rates result in different profile shapes and even more pronounced isotope fractionation ($\Delta^{62/60}Ni_{kam\text{-}tae} > 2.5‰$). Even if a β coefficient of ~0.32 is assumed, as determined by Watson et al. (2016), which results in larger predicted fractionation compared to earlier models that assumed a β of 0.25 (Dauphas, 2007), the conclusions obtained from the measured profiles

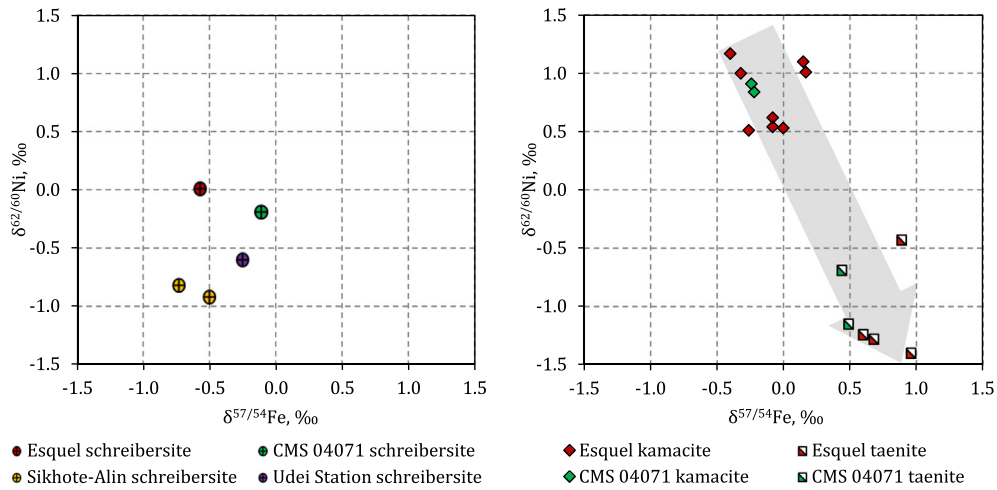

Fig. 7. Isotope plots of $\delta^{57/54}$Fe versus $\delta^{62/60}$Ni for schreibersite grains (left) and kamacite-taenite interfaces (right). Note the negative correlation of the Fe and Ni isotopic signatures as a result of the diffusive isotope fractionation control during kamacite-taenite growth (grey arrow), while schreibersites show no such correlation.

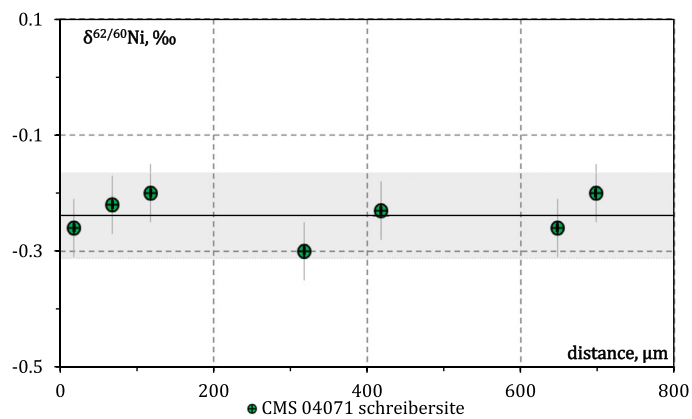

Fig. 8. $\delta^{62/60}$Ni across a single massive schreibersite grain of PMG CMS 04071, adjacent to kamacite Fe-Ni metal (left side of the plot) and olivine (right side of the plot). The solid line and grey bar denote the mean $\delta^{62/60}$Ni = −0.239‰ with 2 standard deviation uncertainty (2 SD = 0.074‰, $n = 7$).

in this work remain valid. Here, β is the coefficient relating the diffusion coefficients of the isotopes to their masses, following $D_1/D_2 = (m_2/m_1)^{\beta}$. Significant improvements in the lateral resolution are needed to quantitatively compare experimental results with the most sharp of the theoretically predicted diffusion-driven isotope ratio profiles. The highest lateral resolution (10 µm) for Fe-Ni isotope ratio measurements in metal was recently achieved using secondary ion mass spectrometry (Watson et al., 2016). Alternatively, the lateral resolution of *fs*-LA-MC-ICP-MS could be enhanced by mathematical deconvolution of isotopic signatures of overlapping line scans (Van Malderen et al., 2015).

Unexpectedly, six measurements of Chinga metal reveal a variability in $\delta^{56/54}$Fe of 0.32‰ (Fig. 5 and the appendix), while laterally resolved isotopic signatures of Ni in the same section of Chinga metal show no significant differences, with a variability in $\delta^{62/60}$Ni of 0.03‰ only. Sub-solidus diffusion between kamacite and taenite cannot be invoked to explain this pattern, as Chinga is an ataxite with no Widmanstätten pattern, previously classified as a IVB member, but currently ungrouped according to the meteoritical bulletin (Chernonozhkin et al., 2014). One of the minerals, the presence of which could influence the Fe isotopic composition but not the Ni isotopic signature, is troilite, as it contains Fe as a major element but has only insignificant amounts of Ni. However, the µXRF maps of this meteorite section confirm that it does not contain any taenite lamellae, troilite, or any other minerals and that the constituting major elements (Fe, Ni) are homogeneously distributed. As such, the observed Fe isotope fractionation could reflect a currently unidentified process driving Fe isotope fractionation, secondary to sub-solidus diffusion.

4.2. Equilibrated olivines in PMG

The abundances of major and several trace elements in olivines of PMGs have previously been shown to be distributed nearly uniformly, with only faint zoning observed

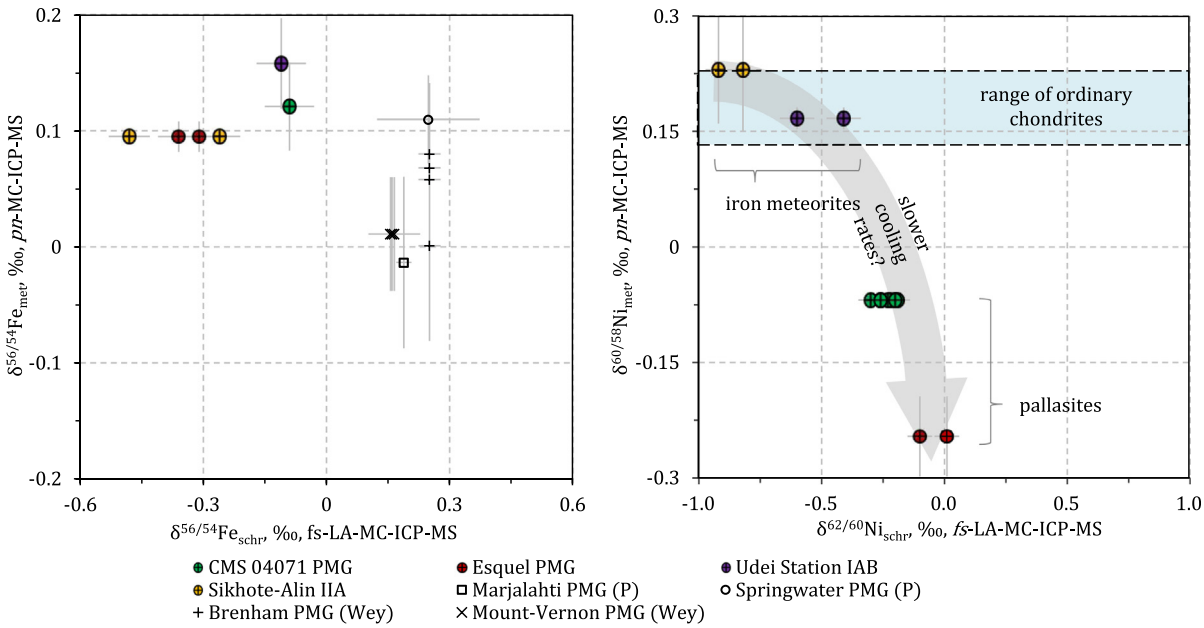

Fig. 9. Fe and Ni isotope ratio plots of schreibersite (measured *via fs*-LA-MC-ICP-MS) *versus* bulk metal, composed of troilite, schreibersite and predominantly of Fe-Ni metal (measured *via* pneumatic nebulization MC-ICP-MS; Chernonozhkin et al., 2016), for two PMGs and two iron meteorites. Literature data for four additional PMGs are also shown: P – (Poitrasson et al., 2005) and Wey – (Weyer et al., 2005). The bulk Ni isotopic data are expressed as $\delta^{60/58}$Ni, although the mass difference for the isotope couples ^{60}Ni-^{58}Ni and ^{62}Ni-^{60}Ni is nearly the same. The $\delta^{60/58}$Ni range for ordinary chondrites is taken from Chernonozhkin et al. (2016).

within a few hundred micrometers of the olivine crystal edges (Miyamoto, 1997). Such zoning is the result of a cooling regime, which provided enough time for sub-solidus diffusion to take place, but was still fast enough to hinder complete homogenization. Such zoning can be used to constrain the cooling rates of the olivines, provided that the diffusion coefficients are known. Using EMPA, both normal concentration patterns, with increased Fe concentrations next to the olivine rim, and reversed Fe concentration patterns have previously been reported within olivines of a single pallasite, both constraining the pallasites cooling rates to within 20–200 °C/yr, in the temperature range of 1100–600 °C (Miyamoto, 1997). For cooling from 1100 °C downwards, the best-fit cooling rate of 2 °C/yr for Fe-Mg zoning in an Esquel olivine was calculated by Miyamoto et al. (2004). However, the Fe concentration variations near the edge of PMG olivines is on the level of the instrumental precision, of the order of 1 at.% Fa#. Tomiyama and Huss (2006) employed a one-dimensional spherical diffusion equation and fitted this theoretical curve to the ion probe concentration gradients of Ca and Co in PMG olivines, which yielded slightly slower cooling rates of 10^{-1} to 10^{2} °C/yr at 1100 °C. For Esquel, Tomiyama and Huss (2006) calculated olivine cooling rates of 10^{-1} to 10^{0} °C/yr. In this work, no Fe-Mg concentration gradients were found in olivines of Brahin, Brenham, CMS 04071, Fukang, Imilac and Seymchan PMGs (Fig. 3D, see the appendix for the EMPA concentration data). The only PMG that shows a Fe-Mg concentration gradient is Esquel, with an olivine core Fa# of 11.23 ± 0.10 at.% (2SD, average of 12 measurements 0.7–3 mm from the rim). This is significantly higher than the average of the olivine rim Fa# (11.11 ± 0.14 at.%, 2SD, average of 9 measurements 0–0.3 mm from the rim) at the 90% confidence level (Student's test $t = 2.011 > t_{19,90\%} = 1.729$). It was recently shown that incomplete diffusive equilibration of olivine is accompanied by kinetically controlled Fe and Mg isotope fractionation, which, in combination with concentration zoning, distinguishes various processes of magmatic olivine formation, for example through crystal growth/dissolution, producing a diffusive boundary layer around the growing crystal, or Fe-Mg inter-diffusion (Sio et al., 2013; Oeser et al., 2015). At the same time, the assumption of full Fe isotopic equilibration between the olivine and metal parts of pallasites allows the equilibration temperatures of these mineral phases to be determined (Poitrasson et al., 2005; Chernonozhkin et al., 2016). Fig. 3 shows four Fe isotope ratio profiles across olivines of two PMG meteorites, while the most itemized olivine profile (Esquel olivine 1) is also complemented by Fe isotopic analysis of kamacite in direct contact to this olivine.

All the data points of the most itemized Esquel olivine 1 profile fall within the ±2 SD range of the olivine $\delta^{56/54}$Fe analysis results ($\delta^{56/54}$Fe = −0.179 ± 0.081‰ for 14 analyses of the Esquel olivine 1 profile), which is similar to the internal precision of the isotope ratio measurement (2 SD on the working standard during a measurement session of a single day). However, the data points are not distributed randomly compared to this average, as the five data points farthest from the olivine-metal rim are systematically lighter. The average of the olivine core ($\delta^{56/54}$Fe = −0.217 ± 0.036‰, 2 SD, five points near the core of the olivine) is significantly lighter than the average of the spots near the rim ($\delta^{56/54}$Fe = −0.158 ± 0.067‰, 2 SD, nine points adjacent to the olivine rim) at the 95% confidence level (Student's test $t = 3.65 > t_{12,95\%} = 2.18$). This

hints towards slightly lighter Fe in the Esquel olivine core than in the olivine rim because of diffusion. The diffusive origin of the profile is supported by the fact that the elemental and isotopic gradients crudely show the same width. As Esquel olivine shows the most pronounced concentration profile among the PMGs measured, this olivine records the upper limit for diffusive isotopic gradients and the corresponding cooling rates of PMG olivines. The observation that olivines of other PMGs do not demonstrate Fa# zoning may be an effect of the crystallographic orientation on the diffusion coefficient in olivine (Dohmen et al., 2007; Van Orman and Krawczynski, 2015). This profile implies significant equilibration during the PMG parent body cooling. Although an Fe isotopic profile is only observed in a single olivine of Esquel, it is possible that Fe was diffusing from olivine into kamacite, generating a heavy Fe isotopic signature and a Fa# depletion in the olivine rim during olivine - metal equilibration in the PMG parent body. In other words, diffusion could represent partial reduction of the olivine rim during olivine-metal equilibration, as iron moves from olivine (Fe^{2+}) to metallic Fe. This scenario is opposite to that of Roskosz et al. (2006), who suggested PMG parent body oxidation to explain the Fe isotope fractionation observed in metal-olivine system in terms of diffusion. A process in which Fe is reduced in olivine is in agreement with Fe-Mg-Mn diagrams, which indicate that olivines of PMG tend to plot along a line of Fe loss/gain (*cf.* Fig. 2 in Boesenberg et al., 2012). However, the magnitude and precision of the $\delta^{56/54}$Fe profile of the Esquel olivine 1 do not allow to quantitatively fit a diffusion model and to constrain the timing of the olivine formation process.

In contrast, the Fe signatures of the less itemized olivines of PMG CMS 04071 appear lighter towards the metal-olivine rim (Fig. 3B). However, no concentration gradient is observed in these olivines, the olivines of CMS 04071 appear less fresh relative to those of Esquel, and the olivines of CMS 04071 contain a network of cracks (see SEM images of CMS 04071 and Esquel olivines in Supplementary Figs. S1 and S2). This indicates that the primary Fe isotopic signatures of the CMS 04071 olivine may have been affected by terrestrial weathering.

4.3. Olivine-metal equilibration

The processes of partial melting of primitive chondritic material, separation of silicate and metal melts, and metal/silicate equilibration provide a direct bearing on the formation of the metal cores and silicate mantles of asteroid bodies in the early Solar System. Although multiple approaches exist to study isotope equilibration between metal and silicate during core formation, there is currently a gap between the experimental approach studying the equilibration of metal and silicates, studies implementing Mössbauer spectroscopy/NRIXS and the elemental and isotopic characterization of natural samples. A potential pitfall of experimental studies is that they often only deal with the equilibration of melted matter. In the experimental approach, incomplete isotopic equilibration, difficulties in obtaining pure phase separates post-experiment and potential open-system behavior can lead to an underestimation of the apparent fractionation (Shahar et al., 2017). At the same time, spectroscopic studies only describe the behavior of crystalline materials, which is likely not the case during core formation. Observations of isotope fractionation in meteorites thus provide a unique view on the early processes of core formation in small asteroid bodies, but these features are overprinted by secondary processes and disturbed by the presence of accessory mineral phases. Pallasites form a suitable meteorite group to study core formation using Fe isotope fractionation, which can be interpreted in terms of mass balance or isotope thermometry (Poitrasson et al., 2005; Weyer et al., 2005). Other groups of differentiated meteorites are also useful in this context (*e.g.,* ureilites; Barrat et al., 2015). A problem with interpreting metal-olivine isotopic compositions at the pallasite parent body scale is heterogeneity of the composing olivine and metal phases. However, as shown in the previous section, during equilibration, diffusion partly homogenized the Fe concentrations in olivine ($\Delta Fa\#_{core\text{-}rim} \approx 0.1$ at.%), and the Fe isotope fractionation resulting from this diffusive process is barely resolvable and observed only for one particular olivine of Esquel characterized in this work. In terms of bulk olivine analyses, the exchange of Fe and related fractionation of Fe isotopes is negligible, as any influence of the 1 mm isotopically heavier outer layer of the olivine ($\Delta^{56/54}Fe_{rim/core} = 0.059‰$) on the bulk isotopic signature of centimeter-sized olivine grains can be considered negligible. Importantly, the (near) absence of Fe isotopic zoning in the Esquel olivine suggests efficient thermal equilibration of the PMG olivine with bulk metal and validates the assumption of complete isotopic equilibration of Fe in the context of isotope thermometric applications (Chernonozhkin et al., 2016). This implies that the apparent Fe isotope fractionation between metal and olivine of PMGs previously observed using bulk methods, should not be explained by diffusive processes (*e.g.,* Poitrasson et al., 2005; Roskosz et al., 2006), but likely represents equilibration at lower temperatures than those used in experimental studies by Poitrasson et al. (2009) or Hin et al. (2012), who observed nearly no fractionation of Fe isotopes in metal-silicate systems experimentally.

For any interpretation of metal-silicate Fe isotope differentiation to be correct, next to olivine data, substantial volumes of bulk metal have to be sampled, because this bulk metal was affected by kinetic and equilibrium effects at lower temperatures, when schreibersite, troilite, kamacite and taenite started to form. However, because of extremely variable abundances of kamacite/taenite/schreibersite/troilite in different PMG sub-samples, it is difficult to estimate the amount of metal needed for a representative bulk sampling. As an alternative to bulk methods, *in situ* data provide a superior approach to sample pure kamacite, not affected by the presence of taenite, troilite and schreibersite or diffusion effects. Although this does not solve the problem of late re-equilibration between metal phases, *in situ* analysis provides an alternative to study isotope fractionation in the silicate-metal system of meteorites. The $\delta^{56/54}$Fe profile of the kamacite directly next to the Esquel olivine 1 margin indicates that the kamacite metal closely adjacent to the olivine is ~0.14‰ lighter than the kamacite remote

from the olivine margin (Fig. 3A). Although this light isotopic signature of the kamacite adjacent to olivine rim is within the range of the Fe isotopic signatures measured for Esquel kamacite in this work, this signature cannot result from sub-solidus diffusion between kamacite and taenite, as no taenite is located near this particular kamacite-olivine margin (see the highlighted location #1 in Fig. 1). Stable signals during the measurement of this individual kamacite with Fe intensities similar to other kamacite locations confirm sampling of pure kamacite. The Fe isotopic signature of the kamacite adjacent to olivine can as such provide an independent estimate of the equilibrium Fe isotope fractionation in metal-olivine systems, different from that based on bulk analysis (see *in situ* data compared to compilation of bulk Fe isotopic signatures of PMGs in Fig. 4). The $\Delta^{56/54}Fe_{kam\text{-}oliv}$ calculated from this *in situ* approach is 0.008‰. The absence of metal-olivine Fe isotope fractionation outside analytical uncertainties is in agreement with the results of Poitrasson et al. (2009) and Hin et al. (2012), who observed $\Delta^{57/54}Fe_{metal\text{–}silicate} = 0.047 \pm 0.063$‰ at 2000 °C and 7.7 GPa and $\Delta^{57/54}Fe_{metal\text{–}silicate} = 0.01 \pm 0.04$‰ at 1250–1300 °C and 1 GPa, respectively, in liquid metal–liquid silicate equilibration experiments. The small Fe isotope fractionation observed at the contact of metal-olivine phase of Esquel is also in agreement with bulk measurements of PMGs Marjalahty (Poitrasson et al., 2005) and Mount Vernon (Weyer et al., 2005). Alternatively, the light Fe isotopic signature of the kamacite adjacent to the olivine may potentially result from terrestrial weathering (*e.g.,* secondary minerals formed in the presence of water and oxygen) at the thin olivine-metal rim (*cf.*, for example Hezel et al., 2015). In the latter case, the light isotopic signature of the kamacite next to olivine should be neglected, and the $\Delta^{56/54}Fe_{kam\text{-}oliv}$ calculated for Esquel is 0.14‰, in agreement with the metal-silicate equilibration experiments of Roskosz et al. (2006), who observed that Fe in metal is 0.2 ± 0.15 ‰/a.m.u. heavier than the silicate at 1500 °C, ambient pressure and log (fO_2) = −5.

Fig. 4 compiles bulk literature data on $\delta^{56/54}Fe$ for the olivines and metal portions of PMGs, together with the measured *in situ* data in this work. Overall, the compiled frequency distributions of $\delta^{56/54}Fe$ reveal chondritic to slightly lighter Fe isotopic signatures for PMG olivines and chondritic to slightly heavier isotopic signatures for PMG metal. These frequency distributions indicate limited fractionation of Fe isotopes between metal and olivine in the PMG parent body, in agreement with the conclusions of Poitrasson et al. (2005). While the fractionation between olivine and metal at PMG parent body scale seems confined (frequency distributions in Fig. 4), multiple individual pallasites measured by different authors show a tendency towards heavier metal and lighter olivine Fe isotopic compositions (Fig. 4). The compilation of literature data in Fig. 4 indicates that although the Fe isotopic fractionation between olivine and metal has occurred in individual PMGs, the isotopic compositions of PMG olivine and metal cannot result from a single fractionation event of initially chondritic material due to mass balance constraints, as evidenced by skewed Fe isotopic distributions. As such, the PMG parent body may locally display non-chondritic Fe isotopic compositions. This may be a result of impact mixing of evolved magmatic olivine with excavated blocks of solidified metal core (*cf.* for example model suggested by Wasson, 2016). Mixing of excavated metal blocks, potentially with (1) shifted Fe isotopic compositions as a result of the fractional crystallization of a core (Chernonozhkin et al., 2016) and (2) different temperatures because of excavation from different depths, could result in locally inhomogeneous Fe isotopic compositions and temperature regimes.

4.4. Schreibersite: equilibrium or diffusion controlled?

In comparison to previous reports on the Fe isotopic composition of schreibersite in other PMGs (Poitrasson et al., 2005; Weyer et al., 2005; also see the corresponding erratum in Poitrasson, 2007), the schreibersites measured in this work exhibit considerably lower $\delta^{56/54}Fe$ values, relative to chondritic values and the results for PMG metal. Relative to metal phases, the Fe and Ni isotopic signatures of schreibersite grains within each individual meteorite exhibit a smaller variability. The largest difference in $\delta^{56/54}Fe$ for different schreibersite grains within an individual meteorite is found for Sikhote-Alin IIA (0.22‰), while the largest difference in $\delta^{62/60}Ni$ is observed for Udei Station IAB (0.19‰; Fig. 5). Fig. 8 shows a $\delta^{62/60}Ni$ isotope profile across a ~800 μm massive schreibersite grain in the PMG CMS 04071 (see highlighted location #1 in Fig. 2). No Ni isotopic zoning is found within the schreibersite analyzed, with single $\delta^{62/60}Ni$ measurements showing a standard deviation of 0.037‰ ($n = 7$) and a range of ~0.10‰. Also, no negative correlation between the Fe and Ni isotopic signatures of schreibersites, as observed in adjacent kamacite and taenite metal phases (Fig. 7), was observed. Consequently, it is unlikely that Fe-Ni isotopic signatures of schreibersites are generated by pure Fe-Ni exchange diffusion. Based on the crystallographic data for schreibersite by Skála and Císařová (2005), the overall crystal chemistry constraints predict that heavy isotopes of Fe and Ni should concentrate in schreibersite in the case of a purely equilibrium control (the reader is referred to the Section 2 of supplementary material for details), consistent with earlier observations of heavy Fe isotopic signatures for schreibersites. These arguments against a purely equilibrium or purely kinetic isotope fractionation control of the Fe and Ni isotopic signatures indicate complex crystallization histories of these meteorites. The isotope fractionation process is driven by the crystallization of schreibersite within the metal – metal phosphide system, where schreibersite may nucleate in several textural modes in different stability fields of the Fe-Ni-P phase diagram (Clarke and Goldstein, 1978). Schreibersite grains (*e.g.,* massive schreibersites and microrhabdites) are known to have different nucleation kinetics (Geist et al., 2005), with equilibrium or kinetic constraints driving the isotopic fractionation of different schreibersite grains.

The use of Fe in schreibersite-metal system in context of isotope thermometry is complicated, because the various Fe isotope fractionation pathways between multiple mineral

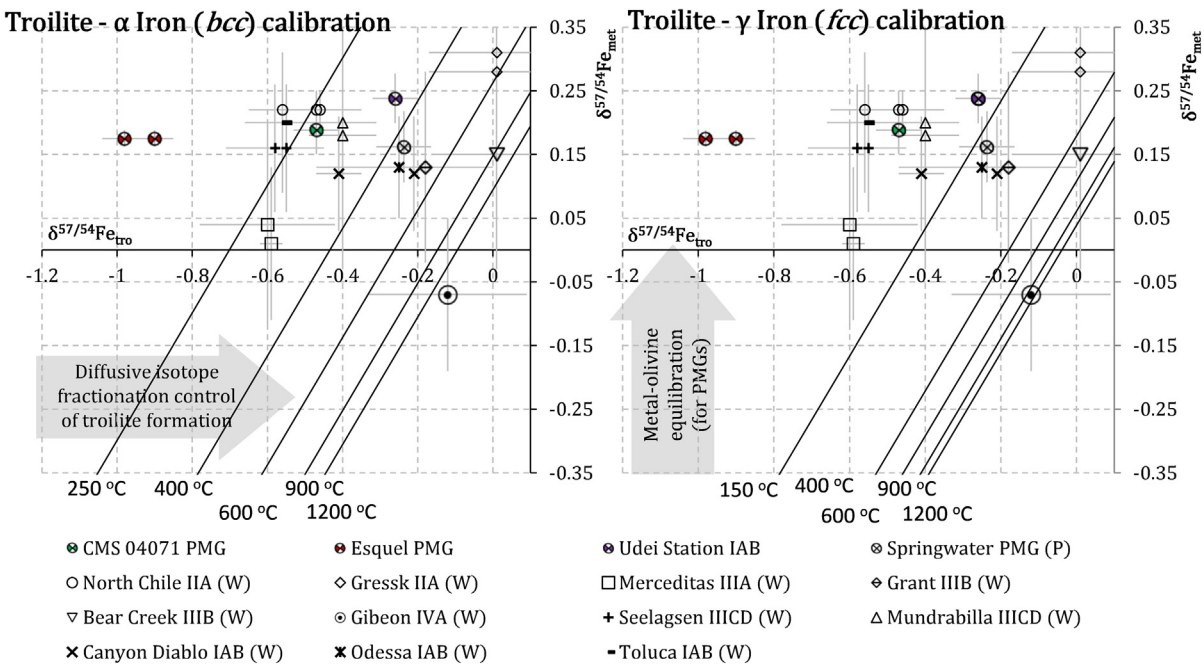

Fig. 10. $\delta^{57/54}Fe_{metal}$ (measured *via* pneumatic nebulization MC-ICP-MS at Ghent University) versus $\delta^{57/54}Fe_{troilite}$ (measured *via fs*-MC-ICP-MS at the Leibnitz University in Hannover) for PMGs and iron meteorites. Geothermometric isotherms at different temperatures are calibrated using parameters based on NRIXS analysis (Dauphas et al., 2012) for *bcc* α – (left) and *fcc* γ – (right) allotropic modifications of Fe-Ni metal. Literature data are taken from: P – (Poitrasson et al., 2005) and W – (Williams et al., 2006). Arrows indicate directions in which Fe isotope ratios may be shifted by processes competitive to troilite-metal equilibration.

phases may mask any clear pattern related to the temperature settings (Fig. 9). In contrast to Fe, Ni is mainly distributed between the metal and the accessory schreibersite. Unlike Fe, the Ni stable isotope ratio signatures of schreibersites in PMGs and iron meteorites show a distinctive trend when plotted versus the bulk metal Ni isotopic compositions (Fig. 9). Fig. 9 indicates that the $\delta^{60/58}$Ni of the bulk metal in PMGs and iron meteorites is negatively correlated with the $\delta^{62/60}$Ni values of schreibersites of the same samples. If schreibersite is fully equilibrated, Ni in the schreibersite-metal system can theoretically be used as an isotopic thermometer, but unfortunately, the isotope fractionation factors or average force constants for the schreibersite-metal system have not yet been studied experimentally. The fractionation of Ni in the metal-schreibersite system explains the light Ni isotopic signatures previously observed in metal of PMG. Previous studies have observed lighter Ni stable isotopic signatures for the metal portions of pallasites relative to the Ni isotope composition of iron meteorites (Cook et al., 2007; Chernonozhkin et al., 2016) and lighter Ni isotopic compositions for pallasite metal compared to those of PMG olivines (Chernonozhkin et al., 2016).

4.5. Assessment of Fe in troilite/metal for isotope thermometry

Sulfur is removed from the Fe-Ni-P-S melts when material of Fe-FeS eutectic composition (troilite) is crystallized at ~1200 °C to the eutectic of 988 °C (Waldner and Pelton, 2005), and the diffusion of Fe is virtually halted at even lower temperatures of ~500 °C (Hin et al., 2012). Troilite does not contain sufficient amounts of Ni to be measured *via* LA-MC-ICP-MS, and only Fe isotopic signatures were measured in troilites of iron meteorites and PMGs (Fig. 5). Two parallel *in situ* measurements of a single troilite grain in PMG Esquel yield nearly identical $\delta^{56/54}$Fe values. Two different troilite grains in the Udei Station IAB iron meteorite also yield nearly identical $\delta^{56/54}$Fe values within analytical uncertainties. This reproducibility suggests that troilites in PMGs and iron meteorites are isotopically equilibrated, and their Fe isotopic signatures are unlikely the result of sub-solidus processes. The Fe isotopic signatures of troilites in iron meteorites and PMGs are isotopically light relative to that of kamacite, with the absolute difference in $\delta^{56/54}$Fe between troilite and bulk metal ($\Delta^{56/54}Fe_{M\text{-}FeS}$) equal to 0.74‰, 0.43‰ and 0.25‰ for Esquel, CMS 04071 and Udei Station, respectively. The observed $\Delta^{56/54}Fe_{M\text{-}FeS}$ strikingly contrast the observations of Hin et al. (2012), who observed no Fe isotope fractionation within analytical uncertainty in their metal – sulfide equilibration experiments. The inconsistency in these results demonstrates that meteoritic troilites remained in isotopic equilibrium with metal at temperatures much lower than those applied by Hin et al. (2012) (*i.e.,* 1250–1300 °C). The maximal $\Delta^{56/54}Fe_{M\text{-}FeS}$ value observed in this work is slightly larger than the $\Delta^{56/54}Fe_{M\text{-}FeS}$ values of 0.53‰, 0.42‰, 0.51‰ and 0.49‰ measured earlier for IIAB, IIIAB, IAB and IIICD irons, respectively (Williams et al., 2006). This agrees with the observed positive correlation between the troilite-metal fractionation factors and the meteorite cooling rates (Williams et al., 2006), as PMGs

were characterized by slower cooling rates relative to iron meteorites. Such correlation between the cooling rate and the isotope fractionation factor indicates thermodynamically driven fractionation, as the closing temperatures and corresponding equilibrated isotope ratios, depend on the diffusive cooling rates through the Dodson equation (Eq. (1)). Experimentally determined average bonding constants for troilites (Dauphas et al., 2012) allow to calculate the temperature dependence of the metal-troilite fractionation. Indeed, the isotherms calculated for Fe isotopes in metal troilite system using the data of Dauphas et al. (2012), yield a range of closure temperatures <900 °C, which is lower than the magmatic temperatures of troilite crystallization in the Fe-FeS system (*i.e.,* ~1200 °C to eutectic 988 °C; Waldner and Pelton, 2005). This is especially the case for the slowest cooling PMGs, independent of the allotrope modification of the Fe-Ni metal with which the troilites equilibrated (α or γ iron; Fig. 10). Although slow cooling rates can extend the range of closure temperatures to lower values (see comment in Section 3 of the supplement), unrealistically low temperatures below 250 °C likely result from disturbances of the Fe isotope ratio data in the troilite-metal system through balancing with other mineral phases (see the directions indicated at Fig. 10). The complexity of the Fe isotope exchange with multiple meteoritic mineral phases other than troilite-metal (Fe mobilized by competitive processes in metal, schreibersite, olivine in the case of PMGs, and multiple silicate phases in the case of IAB complex irons) disturbs any calculation of realistic equilibration temperatures.

5. CONCLUSIONS

Laterally resolved Fe-Ni stable isotopic signatures and lateral isotope ratio profiles, measured *in situ* using *fs*-LA-MC-ICP-MS in various major and minor mineral phases of PMGs and iron meteorites with a spatial resolution of 30–80 μm, indicate overall efficient thermal equilibration of the magmatic mineral phases formed at higher temperatures (olivine, troilite and possibly schreibersite), with predominantly equilibrium-driven isotope fractionation between these phases. This implies that thermodynamics and not kinetics need to be considered in explaining the observed isotopic differences. Olivines, formed in the mantle of the PMG parent body at >>1200 °C, are largely isotopically equilibrated, with only a hint of Fe isotopic zoning in a single olivine of Esquel characterized by a clear concentration gradient, which provides an upper limit to an isotopic diffusion gradient for the PMG olivines. The hint of the Fe isotopic and concentration gradient of crudely comparable width demonstrates Fe loss from olivine in the process of partial reduction of the olivine rim. Efficient Fe isotope equilibration of the olivine permits the use of Fe isotope ratios in the olivine - metal system for isotope geothermometric purposes. However, the complexity of the mineral assemblage of the corresponding metal needs to be taken into account, for example by measuring representative volumes of the bulk metal or by *in situ* measurement of pure kamacite. As evidenced by skewed distributions, olivine and metal Fe isotopic compositions cannot result from a single fractionation event of initially chondritic material following mass balance constraints, but rather represent secondary thermal re-equilibration after catastrophic impact-mixing (*i.e.,* the model described by Wasson (2016)) with localized non-chondritic compositions within the PMG parent body.

The narrow range in Fe isotope ratios measured for troilites ($\delta^{56/54}$Fe of −0.66 to −0.09‰) suggests their efficient thermal equilibration, and their Fe isotopic signatures are unlikely the result of a sub-solidus process. From comparison with available experimental Fe-FeS data, the troilites must have remained in isotopic equilibrium at much lower temperatures long after their crystallization (~1200 °C to 988 °C).

The Ni isotopic signatures of bulk metal and schreibersite correlate negatively, with isotopically lighter Ni in the metal of PMGs and isotopically heavier Ni in the metal of iron meteorites. Such distribution of Ni between metal and phosphide explains the light Ni isotopic signatures previously found for PMG metal and can potentially indicate new relations between the PMG and iron meteorite groups. An equilibrium control on the Fe and Ni isotopic signatures in schreibersite disagrees with the light isotopic signatures observed, because crystal constraints predict that light isotopes should concentrate in the metal. At the same time, no diffusive isotope ratio profiles are found in a massive schreibersite grain, and no negative correlation between the Fe and Ni isotopic signatures is observed, as expected for Fe-Ni diffusive exchange.

In contrast to the phases formed at higher temperatures, kamacite and taenite, exsolved from Fe/Ni metal below ~800 °C, exhibit diffusive Fe and Ni isotope ratio profiles confirming a kinetically driven isotope fractionation mechanism. However, metallographic cooling rates cannot be quantitatively constrained, as the lateral resolution of the diffusive Fe-Ni isotope ratio profiles across the kamacite-taenite interfaces remains insufficient. Still, as the laterally resolved Fe and Ni isotopic signatures across the measured profiles exhibit the largest isotopic shifts farther from the kamacite-taenite interface, the formation of such profiles must have occurred at higher (~650 °C) rather than lower (≤450 °C) temperatures based on a comparison with the theoretically calculated kamacite-taenite sub-solidus diffusive isotope ratio profiles. The comparison of the measured magnitude of kamacite-taenite isotope fractionation of Fe and Ni (*i.e.,* $\Delta^{56/54}Fe_{kam\text{-}tae}$ of −0.51 to −0.69‰ and $\Delta^{62/60}Ni_{kam\text{-}tae}$ of +1.59 to +2.50‰) with the magnitudes predicted by Dauphas (2007) and Watson et al. (2016) allow to broadly constrain the cooling rates of Esquel, CMS 04071 PMGs and Udei Station IAB between ~25 and 500 °C/Myr.

ACKNOWLEDGEMENTS

This research project has been funded by the 'Planet Topers' Interuniversity Attraction Poles Program initiated by the Belgian Science Policy Office. Steven Goderis and Seann J. McKibbin are postdoctoral fellows of the Research Foundation – Flanders. Mona Weyrauch and Stefan Weyer thank for funding by the DFG priority program "The first 10 Million years of the Solar System" (SPP-1385). US Antarctic meteorite samples are recovered by the

Antarctic Search for Meteorites program, which has been funded by NSF and NASA, and characterized and curated by the Department of Mineral Sciences of the Smithsonian Institution and Astromaterials Curation Office at NASA Johnson Space Center. The Research School of Earth Sciences, Australian National University, is thanked for providing an additional pallasite sample. The iron meteorites were kindly donated by Felix P. Lesnov (IGM SB RAS). The FWO-Hercules foundation supported the acquisition of the μXRF instrumentation. The authors acknowledge constructive comments by three anonymous reviewers and associate editor Nicolas Dauphas (University of Chicago).

APPENDIX A. SUPPLEMENTARY MATERIAL

Supplementary data associated with this article can be found, in the online version, at http://dx.doi.org/10.1016/j.gca.2017.08.022.

REFERENCES

Barrat J. A., Rouxel O., Wang K., Moynier F., Yamaguchi A., Bischoff A. and Langlade J. (2015) Early stages of core segregation recorded by Fe isotopes in an asteroidal mantle. *Earth Planet. Sci. Lett.* **419**, 93–100.

Beard B. L. and Johnson C. M. (2004) Fe isotope variations in the modern and ancient earth and other planetary bodies. *Rev. Mineral. Geochem.* **55**, 319–357.

Boesenberg J. S., Delaney J. S. and Hewins R. H. (2012) A petrological and chemical reexamination of Main Group pallasite formation. *Geochim. Cosmochim. Acta* **89**, 134–158.

Chernonozhkin S. M., Goderis S., Bauters S., Vekemans B., Vincze L., Claeys P. and Vanhaecke F. (2014) Evaluation of pneumatic nebulization and ns-laser ablation ICP-MS for bulk elemental analysis and 2-dimensional element mapping of iron meteorites. *J. Anal. At. Spectrom.* **29**, 1001–1016.

Chernonozhkin S. M., Goderis S., Lobo L., Claeys P. and Vanhaecke F. (2015) Development of an isolation procedure and MC-ICP-MS measurement protocol for the study of stable isotope ratio variations of nickel. *J. Anal. At. Spectrom.* **30**, 1518–1530.

Chernonozhkin S. M., Goderis S., Costas-Rodríguez M., Claeys P. and Vanhaecke F. (2016) Effect of parent body evolution on equilibrium and kinetic isotope fractionation: a combined Ni and Fe isotope study of iron and stony-iron meteorites. *Geochim. Cosmochim. Acta* **186**, 168–188.

Clarke R. S. and Goldstein J. I. (1978) Schreibersite growth and its influence on the metallography of coarse-structured iron meteorites. *Smithson. Contrib. Earth Sci.*, 1–80.

Cook D. L., Wadhwa M., Clayton R. N., Dauphas N., Janney P. E. and Davis A. M. (2007) Mass-dependent fractionation of nickel isotopes in meteoritic metal. *Meteorit. Planet. Sci.* **42**, 2067–2077.

Craddock P. R. and Dauphas N. (2011) Iron isotopic compositions of geological reference materials and chondrites. *Geostand. Geoanal. Res.* **35**, 101–123.

Dauphas N. (2007) Diffusion-driven kinetic isotope effect of Fe and Ni during formation of the Widmanstätten pattern. *Meteorit. Planet. Sci.* **42**, 1597–1613.

Dauphas N., Craddock P. R., Asimow P. D., Bennett V. C., Nutman A. P. and Ohnenstetter D. (2009) Iron isotopes may reveal the redox conditions of mantle melting from Archean to Present. *Earth Planet. Sci. Lett.* **288**, 255–267.

Dauphas N., Roskosz M., Alp E. E., Golden D. C., Sio C. K., Tissot F. L. H., Hu M. Y., Zhao J., Gao L. and Morris R. V. (2012) A general moment NRIXS approach to the determination of equilibrium Fe isotopic fractionation factors: application to goethite and jarosite. *Geochim. Cosmochim. Acta* **94**, 254–275.

Dodson M. H. (1973) Closure temperature in cooling geochronological and petrological systems. *Contrib. Mineral. Petrol.* **40**, 259–274.

Dohmen R., Becker H.-W. and Chakraborty S. (2007) Fe–Mg diffusion in olivine I: experimental determination between 700 and 1200 °C as a function of composition, crystal orientation and oxygen fugacity. *Phys. Chem. Miner.* **34**, 389–407.

Drake M. J. and Righter K. (2002) Determining the composition of the Earth. *Nature* **416**, 39–44.

Geist V., Wagner G., Nolze G. and Moretzki O. (2005) Investigations of the meteoritic mineral (Fe, Ni)3P. *Cryst. Res. Technol.* **40**, 52–64.

Goldstein J. I. and Ogilvie R. E. (1965) The growth of the Widmanstätten pattern in metallic meteorites. *Geochim. Cosmochim. Acta* **29**, 893–920.

Greenwood R. C., Franchi I. A., Jambon A., Barrat J. A. and Burbine T. H. (2006) Oxygen isotope variation in stony-iron meteorites. *Science* **313**, 1763–1765.

Hezel D. C., Needham A. W., Armytage R., Georg B., Abel R. L., Kurahashi E., Coles B. J., Rehkämper M. and Russell S. S. (2010) A nebula setting as the origin for bulk chondrule Fe isotope variations in CV chondrites. *Earth Planet. Sci. Lett.* **296**, 423–433.

Hezel D. C., Poole G. M., Hoyes J., Coles B. J., Unsworth C., Albrecht N., Smith C., Rehkämper M., Pack A., Genge M. and Russell S. S. (2015) Fe and O isotope composition of meteorite fusion crusts: possible natural analogues to chondrule formation? *Meteorit. Planet. Sci.* **50**, 229–242.

Hin R. C., Schmidt M. W. and Bourdon B. (2012) Experimental evidence for the absence of iron isotope fractionation between metal and silicate liquids at 1GPa and 1250–1300 °C and its cosmochemical consequences. *Geochim. Cosmochim. Acta* **93**, 164–181.

Horn I., von Blanckenburg F., Schoenberg R., Steinhoefel G. and Markl G. (2006) In situ iron isotope ratio determination using UV-femtosecond laser ablation with application to hydrothermal ore formation processes. *Geochim. Cosmochim. Acta* **70**, 3677–3688.

Horn I. and von Blanckenburg F. (2007) Investigation on elemental and isotopic fractionation during 196 nm femtosecond laser ablation multiple collector inductively coupled plasma mass spectrometry. *Spectrochim. Acta Part B At. Spectrosc.* **62**, 410–422.

Jackson S. E. and Günther D. (2003) The nature and sources of laser induced isotopic fractionation in laser ablation-multicollector-inductively coupled plasma-mass spectrometry. *J. Anal. At. Spectrom.* **18**, 205–212.

Košler J., Pedersen R. B., Kruber C. and Sylvester P. J. (2005) Analysis of Fe isotopes in sulfides and iron meteorites by laser ablation high-mass resolution multi-collector ICP mass spectrometry. *J. Anal. At. Spectrom.* **20**, 192–199.

McKibbin S. J., O'Neill H. S. C., Mallmann G. and Halfpenny A. (2013) LA-ICP-MS mapping of olivine from the Brahin and Brenham meteorites: complex elemental distributions in the pallasite olivine precursor. *Geochim. Cosmochim. Acta* **119**, 1–17.

Miyamoto M. (1997) Chemical zoning of olivine in several pallasites. *J. Geophys. Res.* **102**, 21613–21618.

Miyamoto, M., Koizumi, E., Monkawa, A., Mikouchi, T., 2004. Evaluation of the cooling rate calculated by diffusion modification of Fe-Mg and CaO zoning of pallasite olivine. In: 67th Annual Meteoritical Society Meeting, p. 5119.

Needham A. W., Porcelli D. and Russell S. S. (2009) An Fe isotope study of ordinary chondrites. *Geochim. Cosmochim. Acta* **73**, 7399–7413.

Oeser M., Weyer S., Horn I. and Schuth S. (2014) High-precision Fe and Mg isotope ratios of silicate reference glasses determined in situ by femtosecond LA-MC-ICP-MS and by solution nebulisation MC-ICP-MS. *Geostand. Geoanal. Res.* **38**, 311–328.

Oeser M., Dohmen R., Horn I., Schuth S. and Weyer S. (2015) Processes and time scales of magmatic evolution as revealed by Fe–Mg chemical and isotopic zoning in natural olivines. *Geochim. Cosmochim. Acta* **154**, 130–150.

Poitrasson F., Levasseur S. and Teutsch N. (2005) Significance of iron isotope mineral fractionation in pallasites and iron meteorites for the core–mantle differentiation of terrestrial planets. *Earth Planet. Sci. Lett.* **234**, 151–164.

Poitrasson F. (2007) Does planetary differentiation really fractionate iron isotopes? *Earth Planet. Sci. Lett.* **256**, 484–492.

Poitrasson F., Roskosz M. and Corgne A. (2009) No iron isotope fractionation between molten alloys and silicate melt to 2000 °C and 7.7 GPa: experimental evidence and implications for planetary differentiation and accretion. *Earth Planet. Sci. Lett.* **278**, 376–385.

Povarnitsyn M. E., Itina T. E., Sentis M., Khishchenko K. V. and Levashov P. R. (2007) Material decomposition mechanisms in femtosecond laser interactions with metals. *Phys. Rev. B* **75**, 235414-1–235414-5.

Reed S. J. B., Scott E. R. D. and Long J. V. P. (1979) Ion microprobe analysis of olivine in pallasite meteorites for nickel. *Earth Planet. Sci. Lett.* **43**, 5–12.

Roskosz M., Luais B., Watson H. C., Toplis M. J., Alexander C. M. O. D. and Mysen B. O. (2006) Experimental quantification of the fractionation of Fe isotopes during metal segregation from a silicate melt. *Earth Planet. Sci. Lett.* **248**, 851–867.

Rubie D. C., Jacobson S. A., Morbidelli A., O'Brien D. P., Young E. D., de Vries J., Nimmo F., Palme H. and Frost D. J. (2015) Accretion and differentiation of the terrestrial planets with implications for the compositions of early-formed Solar System bodies and accretion of water. *Icarus* **248**, 89–108.

Russell W. A., Papanastassiou D. A. and Tombrello T. A. (1978) Ca isotope fractionation on the Earth and other solar system materials. *Geochim. Cosmochim. Acta* **42**, 1075–1090.

Schoenberg R. and von Blanckenburg F. (2006) Modes of planetary-scale Fe isotope fractionation. *Earth Planet. Sci. Lett.* **252**, 342–359.

Scott E. R. D. (1972) Chemical fractionation in iron meteorites and its interpretation. *Geochim. Cosmochim. Acta* **36**, 1205–1236.

Shahar A., Elardo S. M. and Macris C. A. (2017) Equilibrium fractionation of non-traditional stable isotopes: an experimental perspective. *Rev. Mineral. Geochem.* **82**, 65–83.

Sio C. K. I., Dauphas N., Teng F.-Z., Chaussidon M., Helz R. T. and Roskosz M. (2013) Discerning crystal growth from diffusion profiles in zoned olivine by in situ Mg–Fe isotopic analyses. *Geochim. Cosmochim. Acta* **123**, 302–321.

Sio C. K. I. and Dauphas N. (2017) Thermal and crystallization histories of magmatic bodies by Monte Carlo inversion of Mg-Fe isotopic profiles in olivine. *Geology* **45**, 67–70.

Skála R. and Císařová I. (2005) Crystal structure of meteoritic schreibersites: determination of absolute structure. *Phys. Chem. Miner.* **31**, 721–732.

Steinhoefel G., Horn I. and von Blanckenburg F. (2009) Matrix-independent Fe isotope ratio determination in silicates using UV femtosecond laser ablation. *Chem. Geol.* **268**, 67–73.

Tanimizu M. and Hirata T. (2006) Determination of natural isotopic variation in nickel using inductively coupled plasma mass spectrometry. *J. Anal. At. Spectrom.* **21**, 1423–1426.

Tomiyama, T., Huss, G.R., 2006. Minor and trace element zoning in pallasite olivine: modeling pallasite thermal history. In 37th Annual Lunar and Planetary Science Conference, pp. 1–2.

Valley J. W. (2001) Stable isotope thermometry at high temperatures. *Rev. Mineral. Geochem.* **43**, 365–413.

Van Malderen S. J. M., van Elteren J. T. and Vanhaecke F. (2015) Submicrometer imaging by laser ablation-inductively coupled plasma mass spectrometry via signal and image deconvolution approaches. *Anal. Chem.* **87**, 6125–6132.

Van Orman J. A. and Krawczynski M. J. (2015) Theoretical constraints on the isotope effect for diffusion in minerals. *Geochim. Cosmochim. Acta* **164**, 365–381.

Van Roosbroek N., Debaille V., Pittarello L., Goderis S., Humayun M., Hecht L., Jourdan F., Spicuzza M. J., Vanhaecke F. and Claeys P. (2015) The formation of IIE iron meteorites investigated by the chondrule-bearing Mont Dieu meteorite. *Meteorit. Planet. Sci.* **50**, 1173–1196.

Waldner P. and Pelton A. D. (2005) Thermodynamic modeling of the Fe-S system. *J. Phase Equilibr. Diffus.* **26**, 23–38.

Wasson J. T. (2016) Formation of the Treysa quintet and the main-group pallasites by impact-generated processes in the IIIAB asteroid. *Meteorit. Planet. Sci.* **51**, 773–784.

Watson H. C., Richter F., Liu A. and Huss G. R. (2016) Iron and nickel isotope fractionation by diffusion, with applications to iron meteorites. *Earth Planet. Sci. Lett.* **451**, 159–167.

Weyer S., Anbar A. D., Brey G. P., Munker C., Mezger K., Woodland A. B., Münker C., Mezger K. and Woodland A. B. (2005) Iron isotope fractionation during planetary differentiation. *Earth Planet. Sci. Lett.* **240**, 251–264.

Weyrauch M., Oeser M., Brüske A. and Weyer S. (2017) In situ high-precision Ni isotope analysis of metals with femtosecond LA-MC-ICP-MS. *J. Anal. At. Spectrom.* **32**, 1312–1319.

Williams H. M., Markowski A., Quitté G., Halliday A. N., Teutsch N. and Levasseur S. (2006) Fe isotope fractionation in iron meteorites: new insights into metal-sulphide segregation and planetary accretion. *Earth Planet. Sci. Lett.* **250**, 486–500.

Zhu X. K., Guo Y., O'Nions R. K., Young E. D. and Ash R. D. (2001) Isotopic homogeneity of iron in the early solar nebula. *Nature* **412**, 311–313.

Associate Editor: Nicolas Dauphas